INSTITUTO FEDERAL
Pernambuco

RELATÓRIO DE ATIVIDADES DESENVOLVIDAS
SEMESTRE 2020.1

CAMPUS: Pesqueira	COORDENAÇÃO: Engenharia Elétrica	
PROFESSOR: Helber Elias Paz de Souza	GRUPO: II	REGIME DE TRABALHO: ( ) 20h ( ) 40h (X) DE

TODAS AS ATIVIDADES DESENVOLVIDAS DEVERÃO SER COMPROVADAS (ART. 21)

ATIVIDADES DE ENSINO (Listar disciplinas ministradas, orientações a alunos concluídas no decorrer do semestre ou em andamento, horários disponibilizados para o atendimento a alunos e demais atividades de ensino descritas no PIT**)**
Conclusão de três disciplinas:
Introdução à Teoria do Controle (6 ENG ELE);
Controle e Acionamentos de Máquinas (8 ELE - MI);
Controle e Acionamentos de Máquinas 1 (3 ELE - PM).
Orientação de um estudante de iniciação científica (Vítor Bismark Ferreira de Macêdo).
Atendimentos aos estudantes realizados após a aula ou no decorrer da semana através do
aplicativo *Google Sala de Aula*, *e-mail* ou conforme as necessidades dos estudantes.
Participação em reuniões do Núcleo Docente Estruturante (NDE) do curso de bacharelado
em engenharia elétrica (Portaria 166/2019 DGCP).
Participação em reuniões do Colegiado do curso de bacharelado em engenharia elétrica
(Portaria 165/2019 DGCP).
Participação em reuniões referentes ao curso técnico em eletrotécnica.
Atividades de apoio ao ensino: reuniões semanais de planejamento pedagógico.
Atividades de apoio ao ensino: organização de eventos direcionados ao corpo discente da instituição.

ATIVIDADES DE PESQUISA (Relatar o andamento dos projetos e demais atividades de pesquisa aplicada listadas no PIT. No caso de projetos, indicar o cronograma de execução (prazos atuais) e as atividades desenvolvidas no decorrer do semestre**)**
Atuação como membro de projeto de pesquisa e inovação tecnológica em um grupo
(Interdisciplinar em Fontes Renováveis de Energia e Sistemas Eletroeletrônicos Aplicados)
certificado pela instituição (IFPE) junto ao CNPq em efetiva produção.
Um artigo publicado em revista internacional Qualis A1 (Fast Phase Angle Jump Estimation
to Improve the Convergence Time of the GDSC-PLL, *Transactions on Industrial Electronics*,
April 2020, **DOI:** 10.1109/TIE.2019.2913823).
Um artigo publicado em revista internacional Qualis B1 (Complex Controllers Applied to *and*
Space Vectors: A Survey on Characteristics and Advantages, *Journal of Control, Automation*
Electrical Systems, Julho 2020, **DOI:** 10.1007/s40313-020-00623-7).

ATIVIDADES DE EXTENSÃO (Relatar o andamento dos projetos e demais atividades de extensão listadas no PIT. No caso de projetos ou programas, indicar o cronograma de execução (prazos atuais) e as atividades desenvolvidas no decorrer do semestre.**)**
Nada a declarar.

ATIVIDADES ADMINISTRATIVO-PEDAGÓGICAS (Descrever as principais atividades desenvolvidas na gestão institucional do IFPE de acordo com a função; ou atividades em comissões/fiscalizações realizadas no decorrer do semestre de acordo com o PIT**)**
Nada a declarar.

COMPLEMENTO/OBSERVAÇÕES

gov.br Documento assinado digitalmente Helber Elias Paz de Souza Data: 23/11/2020 09:56:38-0300 CPF: 046.153.414-23	gov.br Documento assinado digitalmente Alexandre Manoel de Farias Data: 24/11/2020 17:17:24-0300 CPF: 034.323.294-40	
DOCENTE	**COORDENAÇÃO**	**DEPARTAMENTO**

MANOEL HENRIQUE DE OLIVEIRA PEDROSA FILHO: 89973917472 Assinado digitalmente por MANOEL HENRIQUE DE OLIVEIRA PEDROSA FILHO:89973917472 DN: C=BR, O=ICP-Brasil, OU=000001009712196, OU=Secretaria da Receita Federal do Brasil - RFB, OU=RFB e-CPF A1, OU=AC SERASA RFB v5, OU=62173620000180, OU=VIDEOCONFERENCIA, CN=MANOEL HENRIQUE DE OLIVEIRA PEDROSA FILHO:89973917472 Razão: Eu estou aprovando este documento Localização: Pesqueira-PE Data: 2021-04-28 07:51:12	gov.br Documento assinado digitalmente Otavio Washington Lima Silva Data: 28/03/2021 20:14:21-0300 CPF: 095.354.834-12	Documento assinado digitalmente Kalina Curie Tenorio Fernandes do Rego Barros Data: 25/03/2021 17:53:05-0300 CPF: 834.052.674-04
DIREÇÃO DE PESQUISA	**DIREÇÃO DE EXTENSÃO**	**DIREÇÃO DE ENSINO**

Q-ACADÊMICO WEB

ENCERRAR SESSÃO

MÓDULO DO PROFESSOR | 2020 | 1 | Muda Ano/Período

Página Inicial > **Meus Diários**

Meus Diários

Meus diários de 2020/1 .

☐ **Exibir somente os diários com etapas não entregues.**

	Diário	CH	Alunos	Opções
282023	Percentual de horas realizadas: 100% **EEPS.39 - INTRODUÇÃO À TEORIA DO CONTROLE (54H/72HA)** **Professor principal**: HELBER ELIAS PAZ DE SOUZA **Turma:** 20201.EEPS.6 **Curso:** ENGENHARIA ELÉTRICA **Turno:** Integral Horário da Turma Envio de perguntas (FAQ - tira-dúvidas): **habilitado** [desabilitar]	54	13	Notas e Faltas Material de Aula

Etapas			
Controle de Avaliações:	UNID1	UNID2	EF
Frequência e Conteúdo:	UNID1	UNID2	
Entrega WEB:	✓	✓	✓
Entrega Física:	✗	✗	✗

Impressão de diários			
☑ Trazer o diário preenchido			
Frequência:	UNID1	UNID2	
Avaliações:	UNID1	UNID2	EF
Frequência com Notas:	UNID1	UNID2	
Conteúdo:	UNID1	UNID2	
Notas Consolidadas:	Diário Notas Consolidadas		

	Diário	CH	Alunos	Opções
282090	Percentual de horas realizadas: 100% **B303402 - CONTROLE E ACIONAMENTO DE MÁQUINAS 1 (60H/80HA)** **Professor principal**: HELBER ELIAS PAZ DE SOUZA **Turma:** 20201.B3-PS.3N **Curso:** ELETROTÉCNICA - SUB **Turno:** Noturno Horário da Turma Envio de perguntas (FAQ - tira-dúvidas): **habilitado** [desabilitar]	60	19	Notas e Faltas Material de Aula

Etapas			
Controle de Avaliações:	UNID1	UNID2	EF
Frequência e Conteúdo:	UNID1	UNID2	EF
Entrega WEB:	✓	✓	✓
Entrega Física:	✗	✗	✗

Impressão de diários			
☑ Trazer o diário preenchido			
Frequência:	UNID1	UNID2	EF
Avaliações:	UNID1	UNID2	EF
Frequência com Notas:	UNID1	UNID2	EF
Conteúdo:	UNID1	UNID2	EF
Notas Consolidadas:	Diário Notas Consolidadas		

	Diário	CH	Alunos	Opções
282080	Percentual de horas realizadas: 100% **B12-PS.099 - CONTROLE E ACIONAMENTO DE MÁQUINAS (67.5H/90HA)** **Professor principal**: HELBER ELIAS PAZ DE SOUZA **Turma:** 20201.B12-PS.8V **Curso:** TÉCNICO EM ELETROTÉCNICA - INTEGRADO **Turno:** Vespertino Horário da Turma Envio de perguntas (FAQ - tira-dúvidas): **habilitado** [desabilitar]	67.5	18	Notas e Faltas Material de Aula

Etapas			
Controle de Avaliações:	UNID1	UNID2	EF
Frequência e Conteúdo:	UNID1	UNID2	
Entrega WEB:	✓	✓	✓
Entrega Física:	✗	✗	✗

Impressão de diários			
☑ Trazer o diário preenchido			
Frequência:	UNID1	UNID2	
Avaliações:	UNID1	UNID2	EF
Frequência com Notas:	UNID1	UNID2	
Conteúdo:	UNID1	UNID2	

Notas Consolidadas: Diário Notas Consolidadas

Legenda

- Etapa com posse do professor
- Etapa com posse do registro
- Etapa com importação automática de notas do Moodle

22/11/2020 HELBER ELIAS PAZ DE SOUZA 2020 1 Muda Ano/Período **Versão 3.287.001** **© 2004 Qualidata**

SERVIÇO PÚBLICO FEDERAL
MINISTÉRIO DA EDUCAÇÃO
INSTITUTO FEDERAL DE EDUCAÇÃO CIÊNCIA E TECNOLOGIA DE PERNAMBUCO
CAMPUS PESQUEIRA

DECLARAÇÃO

O Instituto Federal de Ciência e Tecnologia de Pernambuco- Campus Pesqueira, por meio do Departamento de Inovação, Pesquisa e Pós-Graduação - DIPP declara, para os devidos fins, que **HELBER ELIAS PAZ DE SOUZA** orientou **Vítor Bismark Ferreira de Macedo** no seu plano de atividades intitulado "Sistema embarcado para simulação em tempo real de sistemas elétricos com foco no monitoramento da qualidade da energia elétrica (parte ii)", no período de 1/8/2019 a 31/7/2020.

INSTITUTO FEDERAL DE
EDUCAÇÃO, CIÊNCIA E TECNOLOGIA
PERNAMBUCO
Campus Pesqueira

Pesqueira, 3 de novembro de 2020.

Manoel Henrique de Oliveira Pedrosa Filho
Diretor do Departamento de Inovação Pesquisa e Pós-graduação
Portaria 1.201 DOU nº 173 de 08 de setembro de 2017

SERVIÇO PÚBLICO FEDERAL
MINISTÉRIO DA EDUCAÇÃO
SECRETARIA DE EDUCAÇÃO PROFISSIONAL E TECNOLÓGICA
INSTITUTO FEDERAL DE EDUCAÇÃO, CIÊNCIA
E TECNOLOGIA DE PERNAMBUCO

PORTARIA IFPE/DGCP Nº 166, DE 24 DE OUTUBRO DE 2019

Designa a atualização da composição do Núcleo Docente Estruturante (NDE) do Curso de Bacharelado em Engenharia Elétrica

O DIRETOR-GERAL DO *CAMPUS* Pesqueira, em conformidade.com a solicitação do Oficio Nº 039/2019/CCEE/IFPE, no uso das atribuições que lhe são conferidas pelo Estatuto da Instituição, pela Portaria Nº 566/2016, publicada no D.O.U. de 03/05/2016, folha Nº 83.

I – Processo nº 23299.018054.2019-47

RESOLVE:

Art. 1° Instituir a Comissão denominada de Núcleo Docente Estruturante (NDE) do curso de Bacharelado em Engenharia Elétrica, composta pelos seguintes membros:

Nome	Matrícula	Unidade de Exercício do Membro	Função
Alexandre Manoel de Farias	SIAPE 2181805	IFPE campus Pesqueira	Presidente/Coordenador
Bruno Gomes Moura de Oliveira	SIAPE 1863615	IFPE campus Pesqueira	Representante docente
Charlene Tereza da Silva Dias Leite	SIAPE 1695625	IFPE campus Pesqueira	Representante docente
Helber Elias Paz de Souza	SIAPE 1667857	IFPE campus Pesqueira	Representante docente
Manoel Henrique de Oliveira Pedrosa Filho	SIAPE 1539768	IFPE campus Pesqueira	Representante docente
Marcio Severino da Silva	SIAPE 2164920	IFPE campus Pesqueira	Representante docente
Oberlan da Silva	SIAPE 1654269	IFPE campus Pesqueira	Representante docente
Valdemir Mariano	SIAPE 1181955	IFPE campus Pesqueira	Representante docente
Ygo Neto Batista	SIAPE 1667870	IFPE campus Pesqueira	Representante docente

Art. 2º Compete à Comissão denominada de Núcleo Docente Estruturante (NDE):

I. Atuar no processo de concepção e consolidação do Projeto Pedagógico do Curso;
II. Conduzir os trabalhos de reestruturação curricular, para aprovação no Colegiado de Curso e no Conselho Superior do IFPE;

III. Contribuir para a consolidação do perfil profissional do egresso do curso;
IV. Contribuir para atualização periódica do Projeto Pedagógico do Curso, em consonância com as demandas sociais e os arranjos produtivos locais e regionais;
V. Implantar as políticas institucionais de ensino, pesquisa e extensão no âmbito do curso;
VI. Realizar avaliação periódica do curso, considerando-se as orientações do Sistema Nacional de Avaliação da Educação Superior – SINAES em articulação com o trabalho da CPA, em parceria com a Comissão e Avaliação Preventiva da PRODEN;
VII. Propor ações decorrentes das avaliações realizadas no âmbito do curso em articulação com o trabalho da Comissão Própria de Avaliação – CPA;
VIII. Zelar pelo cumprimento das Diretrizes Curriculares Nacionais.
IX. Recomendar a aquisição de bibliografia e outros materiais necessários ao curso;

Art. 3º A comissão terá duração de 360 dias e se reunirá bimestralmente nas quartas-feiras, em caráter ordinário, e extraordinariamente, sempre que necessário, podendo, nesse caso, a reunião ser requerida pelo Presidente.

§ 1º As proposições dispostas nas reuniões serão aprovadas pela maioria simples de votos dos membros presentes ou quórum mínimo de 3 membros.

§ 2º Em caso de empate, o voto de desempate (ou de qualidade) será exercido pelo Presidente.

§ 3º Fica vedada a divulgação de discussões em curso sem a prévia anuência do Presidente.

§ 4º Nos termos do art. 6º, inciso VI, do Decreto nº 9.759, de 11 de abril de 2019, fica vedada a criação de subcomissões por ato deliberado na reunião.

§ 5º As reuniões cujos membros estejam em estados ou municípios distintos serão realizadas por videoconferência.

Art. 4º As medidas decorrentes das reuniões serão apresentadas ao gestor da unidade administrativa, responsável pelo processo pertinente à comissão, por meio de relatórios mensais ou relatório final das atividades realizadas;

Art. 5º Caberá à unidade administrativa responsável pelo processo prestar o apoio administrativo à comissão.

Art. 6º Caberá ao Presidente, quando necessário, submeter ao Diretor-Geral a estimativa dos gastos com diárias e passagens para os membros da comissão, em observância à disponibilidade orçamentária e financeira para o exercício em curso, na hipótese de ser demonstrada, de modo fundamentado, a inviabilidade ou a inconveniência de se realizar a reunião por videoconferência.

Art. 7º Esta Portaria entra em vigor na data de sua publicação.

VALDEMIR MARIANO

Assinado de forma digital por VALDEMIR MARIANO
Dados: 2019.11.01 15:05:34 -03'00'

Valdemir Mariano
Diretor Geral do IFPE campus Pesqueira
Portaria DOU no. 566 de 03/05/2016

SERVIÇO PÚBLICO FEDERAL
MINISTÉRIO DA EDUCAÇÃO
SECRETARIA DE EDUCAÇÃO PROFISSIONAL E TECNOLÓGICA
INSTITUTO FEDERAL DE EDUCAÇÃO, CIÊNCIA
E TECNOLOGIA DE PERNAMBUCO

PORTARIA IFPE/DGCP Nº 165, DE 24 DE OUTUBRO DE 2019

Designa a atualização da composição do Colegiado do Curso de Bacharelado em Engenharia Elétrica

O DIRETOR-GERAL DO *CAMPUS* Pesqueira, em conformidade.com a solicitação do Oficio Nº 38/2019/CCEE/IFPE, no uso das atribuições que lhe são conferidas pelo Estatuto da Instituição, pela Portaria Nº 566/2016, publicada no D.O.U. de 03/05/2016, folha Nº 83.

I – Processo nº 23299.018053.2019-19

RESOLVE:

Art. 1° Instituir a Comissão denominada de Colegiado do curso de Bacharelado em Engenharia Elétrica, composta pelos seguintes membros:

Nome	Matrícula	Unidade de Exercício do Membro	Função
Alexandre Manoel de Farias	SIAPE 2181805	IFPE campus Pesqueira	Presidente/Coordenador
Anderson Lucian da Silva	SIAPE 1095235	IFPE campus Pesqueira	Téc. em Assuntos Educacionais
Monique Maria Batista De Oliveira	SIAPE 2322077	IFPE campus Pesqueira	Pedagoga
Pedro Henrique Dules de Lima	20172EEPS0303	IFPE campus Pesqueira	Representante estudante
Airlan Arnaldo Nascimento de Lima	SIAPE 1582413	IFPE campus Pesqueira	Representante docente
Alexandre Valença do Nascimento Silva	SIAPE 1668649	IFPE campus Pesqueira	Representante docente
Bruno Gomes Moura de Oliveira	SIAPE 1863615	IFPE campus Pesqueira	Representante docente
Bruno Lopes Oliveira da Silva	SIAPE 1934852	IFPE campus Pesqueira	Representante docente
Carlos Bino de Souza	SIAPE1961071	IFPE campus Pesqueira	Representante docente
Charlene Tereza da Silva Dias Leite	SIAPE 1695625	IFPE campus Pesqueira	Representante docente

Cícero Jailton de Moraes Souza	SIAPE 1160058	IFPE campus Pesqueira	Representante docente
Erivaldo Ferreira De Morais Júnior	SIAPE 1390416	IFPE campus Pesqueira	Representante docente
Fabiana Julia de Araújo Tenório	SIAPE 2459684	IFPE campus Pesqueira	Representante docente
Filipe Andrade de Lucena	SIAPE 3087834	IFPE campus Pesqueira	Representante docente
Jandrews Lins Gomes	SIAPE 1058115	IFPE campus Pesqueira	Representante docente
José Daniel Soares de Paiva	SIAPE 2168924	IFPE campus Pesqueira	Representante docente
Josineide Braz de Miranda Lira	SIAPE 1100719	IFPE campus Pesqueira	Representante docente
Kleber Fernando Rodrigues	SIAPE 1080107	IFPE campus Pesqueira	Representante docente
Leonardo Moura de Amorim	SIAPE 1803483	IFPE campus Pesqueira	Representante docente
Magda Cristina Pedroza Tavares	SIAPE 1746983	IFPE campus Pesqueira	Representante docente
Manoel Henrique de Oliveira Pedrosa Filho	SIAPE 1539768	IFPE campus Pesqueira	Representante docente
Márcio Severino da Silva	SIAPE 2164920	IFPE campus Pesqueira	Representante docente
Marlesson Castelo Branco Do Rego	SIAPE 1207889	IFPE campus Pesqueira	Representante docente
Oberlan da Silva	SIAPE 1654269	IFPE campus Pesqueira	Representante docente
Regina Maria de Lima Neta	SIAPE 1409373	IFPE campus Pesqueira	Representante docente
Rhafael Roger Pereira	SIAPE1812582	IFPE campus Pesqueira	Representante docente
Ricardo Gomes Duarte Freire	SIAPE 3131891	IFPE campus Pesqueira	Representante docente
Rossana Manuela do Monte	SIAPE 3009024	IFPE campus Pesqueira	Representante docente
Tulio Albuquerque Dias	SIAPE 1169873	IFPE campus Pesqueira	Representante docente
Ygo Neto Batista	SIAPE 1667870	IFPE campus Pesqueira	Representante docente

Art. 2º Compete à Comissão denominada de Colegiado:

I. analisar e validar o Projeto Pedagógico do Curso para encaminhá-lo à Direção de Ensino;
II. acompanhar a execução didático-pedagógica do Projeto Pedagógico do Curso;
III. propor oferta de turmas, aumento ou redução do número de vagas, a serem publicados em edital de seleção, em consonância com o Plano de Desenvolvimento Institucional (PDI) e observando os recursos humanos, materiais e didáticos existentes no IFPE;
IV. propor modificações no Projeto Pedagógico do Curso e nos Programas dos Componentes Curriculares;
V. apreciar e aprovar os planos de atividades a serem desenvolvidos em cada ano letivo, comunicando, na época devida, à Direção de Ensino ou instância equivalente;
VI. promover a integração das atividades de ensino, pesquisa e extensão do curso;
VII. deliberar sobre questões relativas à vida acadêmica, tais como frequência, equivalência e adaptações de estudos, exames e avaliações de acordo com a Organização Acadêmica;
VIII. atuar de forma consultiva e deliberativa, em primeira instância, na área do Ensino, Pesquisa e Extensão;
IX. elaborar o cronograma de liberação de professores no âmbito do Colegiado, para participação em cursos de aperfeiçoamento, qualificação profissional em nível de Especialização, Mestrado, Doutorado e Pós-doutorado, de acordo com o Plano Institucional de Capacitação do Servidor (PIC);
X. apoiar os processos de avaliação do curso, fornecendo as informações necessárias;

Art. 3º A comissão terá duração de 360 dias e se reunirá bimestralmente nas quartas-feiras, em caráter ordinário, e extraordinariamente, sempre que necessário, podendo, nesse caso, a reunião ser requerida pelo Presidente.

§ 1º As proposições dispostas nas reuniões serão aprovadas pela maioria simples de votos dos membros presentes ou quórum mínimo de 8 membros.

§ 2º Em caso de empate, o voto de desempate (ou de qualidade) será exercido pelo Presidente.

§ 3º Fica vedada a divulgação de discussões em curso sem a prévia anuência do Presidente.

§ 4º Nos termos do art. 6º, inciso VI, do Decreto nº 9.759, de 11 de abril de 2019, fica vedada a criação de subcomissões por ato deliberado na reunião.

§ 5º As reuniões cujos membros estejam em estados ou municípios distintos serão realizadas por videoconferência.

Art. 4º As medidas decorrentes das reuniões serão apresentadas ao gestor da unidade administrativa, responsável pelo processo pertinente à comissão, por meio de relatórios mensais ou relatório final das atividades realizadas;

Art. 5º Caberá à unidade administrativa responsável pelo processo prestar o apoio administrativo à comissão.

Art. 6º Caberá ao Presidente, quando necessário, submeter ao Diretor-Geral a estimativa dos gastos com diárias e passagens para os membros da comissão, em observância à disponibilidade orçamentária e financeira para o exercício em curso, na hipótese de ser demonstrada, de modo fundamentado, a inviabilidade ou a inconveniência de se realizar a reunião por videoconferência.

Art. 7º Esta Portaria entra em vigor na data de sua publicação.

Valdemir Mariano
Diretor Geral do IFPE campus Pesqueira
Portaria DOU no. 566 de 03/05/2016

SERVIÇO PÚBLICO FEDERAL
MINISTÉRIO DA EDUCAÇÃO E DO DESPORTO
SECRETARIA DE EDUCAÇÃO MÉDIA E TECNOLÓGICA
INSTITUTO FEDERAL DE EDUCAÇÃO, CIÊNCIA E TECNOLOGIA DE PERNAMBUCO
CAMPUS PESQUEIRA
Autorização para funcionamento Portaria nº. 1533, de 19/10/92 - MEC
Loteamento Portal, BR 232 - Km 214 - Pesqueira - PE - Telefax (87) 3835-1796

COORDENAÇÃO DE ELETROTÉCNICA

ATAS DE REUNIÃO

Período: Abril/20 – Set/20

Horário: 19:00

Local: Google Meet

CHAMADA

As reuniões de Área do curso de Eletrotécnica do IFPE Campus Pesqueira durante o semestre 2020.1, foram realizadas no período de Abril/20 a Set/2020, no Google Meet. Com início às 19:00 e foram presididas por Regina Maria de Lima Neta.

- **Nome dos Participantes**

Docente	SIAPE
Alexandre Manoel de farias	2181805
Antonio Cabral dos Santos	2964281
Bruno Albuquerque Dias	1326008
Bruno Gomes Moura de Oliveira	1863615
Edson Ricardo Sabino Calado	1959205
Fernando Edier França de Freitas	2789484
Filipe Lucena Medeiros de Andrade	3087834
Gilmario dos Anjos Lima	2477469
Helber Elias Paz de Souza	1667857
Kal-El Basilio Brito	1246084
Manoel Henrique de Oliveira P. Filho	1539768
Marlesson Castelo Branco do Rego	1207889
Regina Maria de Lima Neta	1409373
Túlio Albuquerque Dias	1169873
Ygo Batista Neto	1667870

- **Data das Reuniões**

Evento	Data
Reunião	13/04/20
Reunião	20/04/20
Webinar com o Profº Filipe Lucena. “Efeito do Acoplamento Mútuo dos Fenômenos Térmicos e Mecânicos no Enrolamento de Transformadores de Potência”.	27/04/20
Webinar com o Profº Kal-El Basílio. “Caracterização do Estado Operacional de Isoladores Poliméricos por Atributos Selecionados de Vídeos UV - Visão Geral”.	04/05/20
Webinar com o Profº Bruno Dias. “Gestão Técnica de Isoladores Poliméricos Utilizando Aprendizado de Máquina”.	11/05/20
Webinar com o Profº Edson Ricardo. “Metodologia de Previsão de Radiação Solar e Temperatura Ambiente Voltada para Auxiliar Previsões de Geração de Usinas Fotovoltaicas”.	18/05/20
Webinar com o Profº Ygo Batista. “Projeto Total Sky Imager –Resultados Iniciais”.	25/05/20
Bate-papo com Profissional com o Profº Bruno Oliveira. “Oportunidades Profissionais na Àrea de Engenharia Clínica em PE”.	28/05/20
Webinar com o Profº Fernando Edier. “Estudos de Transitórios Eletromagnéticos”.	01/06/20
Bate-papo com Profissional os Profº Edson Ricardo e Fernando Edier. “Dia-a-dia do Profissional da Elétrica na CHESF”.	04/06/20
Webinar com Profº Helber de Souza. “Filtros Digitais. GDSC – Cancelamento por Sinal Atrasado Generalizado”.	08/06/20
Bate-papo com Profissional com o Profº Filipe Lucena. “Certificação e Engenharia de Processos. O que é e quais as oportunidades?”	11/06/20
Webinar Profº Tulio Dias: Inversores Aplicados a Sistemas Fotovoltaicos com Baterias – Topologia Híbrida.	15/06/20
Bate-papo com Profissional Profº Gilmário Lima: O Engenheiro e a Perícia Criminal.	18/06/20
Webinar com o Profº Manoel Henrique: A Interdisciplinaridade do Projeto de uma Usina Solar Fotovoltaica.	22/06/20
Bate-papo com Profissional com os técnicos Camila Américo e Eurlles Canuto: Desafios no Dia-a-Dia de um Técnico de Laboratório no IFPE.	25/06/20
Webinar com profº Bruno Oliveira: Aplicações da Engenharia de Micro-ondas no Nosso Cotidiano.	29/06/20
Bate-papo com Profissional com o profº Filipe Lucena: Empresa Junior – como abrir e por que participar.	02/07/20
Webinar com o profº Fernando Edier: Limitadores de Curto-Circuito a Base de Reatores Naturalmente Saturados.	06/07/20
Bate-papo com Profissional com os profs Manoel Henrique e Filipe Lucena: Desenvolvimento de Oportunidades no Campus Pesqueira: Metys e Centro de Referência em Energia Solar.	09/07/20
Webinar com o profº Manoel Henrique: Impactos da Geração Solar Fotovoltaica na Rede Elétrica.	13/07/20
Bate-papo com Profissional com o profº Bruno Dias: Desafios do Dia-a-Dia de um Engenheiro de Obra.	16/07/20
Webinar com o profº Marcio Silva (Campus Garanhuns). “Perdas em Linhas de Transmissão de Energia”.	20/07/20
Bate-papo com o profº Bruno Oliveira. “Regulação Técnica do Setor Elétrico Brasileiro”.	24/07/20

Webinar com o profº Marlo Andrade (Campus Palmares). “Sistema de Interrogação Sem Fio para Sensores Passivos”.	27/07/20
Reunião Final do Semestre Letivo	28/09/20

PAUTAS

- Situação pandemia;
- Atividades remotas;
- Portaria 401 IFPE. Trabalho Docente Remoto;
- Organização de Reuniões Semanais;
- Oferta de monitoria no semestre 2020.2;
- Ofício Nº 210/2020 – PRODEN.

PROPOSTA PRINCIPAL

- Elaboração dos Eventos On-line Semanais: Webinar de Pesquisa, Inovação e Extensão e Bate-papo com Profissional;
- Deliberação referente a organização das disciplinas para o Ensino Remoto.

Pesqueira, 28 de setembro de 2020.

- **Assinaturas**

Docente	SIAPE	Assinatura
Alexandre Manoel de farias	2181805	
Antonio Cabral dos Santos	2964281	
Bruno Albuquerque Dias	1326008	
Edson Ricardo Sabino Calado	1959205	
Fernando Edier França de Freitas	2789484	
Filipe Lucena M. de Andrade	3087834	
Gilmario dos Anjos Lima	2477469	
Helber Elias Paz de Souza	1667857	
Kal-El Basilio Brito	1246084	
Manoel Henrique de Oliveira P. Filho	1539768	
Marlesson Castelo Branco do Rego	1207889	
Regina Maria de Lima Neta	1409373	
Túlio Albuquerque Dias	1169873	
Ygo Batista Neto	1667870	

Regina Mª de Lima Neta

REGINA MARIA DE LIMA NETA
Coordenação do Curso Técnico em Eletrotécnica
Portaria nº. 212, DOU 13/02/2020, seção 2, Pg. 21

Pesquisador(a)

Helber Elias Paz de Souza

Endereço para acessar este espelho: dgp.cnpq.br/dgp/espelhorh/3278243022878251

Dados Gerais

Nome em citações bibliográficas: de SOUZA, H. E. P.; DE SOUZA, H. E. P.; DE SOUZA, HELBER E. P.; SOUZA, HELBER; DE SOUZA, HELBER

Titulação: Doutorado

Áreas de atuação:

Bolsista CNPq:

Última atualização do Currículo Lattes: 07/11/2020

Homepage: pesqueira.ifpe.edu.br

Grupos de pesquisa em que atua

Nome do grupo	Instituição	Perfil
Grupo de Eletrônica de Potência e Acionamentos Elétricos - GEPAE	UFPE	Pesquisador
Interdisciplinar em Fontes Renováveis de Energia e Sistemas Eletroeletrônicos Aplicados	IFPE	Pesquisador

Journal of Control, Automation and Electrical Systems (2020) 31:1132–1152
https://doi.org/10.1007/s40313-020-00623-7

Complex Controllers Applied to Space Vectors: A Survey on Characteristics and Advantages

Rafael C. Neto[1] · Francisco A. S. Neves[1] · Helber E. P. de Souza[2]

Received: 17 May 2019 / Revised: 8 May 2020 / Accepted: 10 June 2020 / Published online: 8 July 2020
© Brazilian Society for Automatics–SBA 2020

Abstract
This work presents the characteristics and advantages of using complex controllers applied to space vectors. A mathematical background is presented to show that the harmonic spectrum of a space vector indicates the phase-sequence of each harmonic that composes this vector. As consequence, a reference space vector can be used for applications in which the control system has three-phase reference signals. This approach allows the implementation of complex controllers that present lower order, require less memory elements and have better dynamic response than real controllers. A literature review is made to enable a structural comparison (in terms of computational cost) between several real and complex control schemes based on the internal model principle. Two experimental applications are used to evaluate the performance of complex controllers.

Keywords Control systems · Complex controller · Space vector · Harmonic compensation

1 Introduction

Due to the increasing demand for renewable energy sources, such as solar and wind energies, a significant increase in the number of three-phase grid-connected inverters has been observed in recent decades. Most applications of these inverters have a structure that includes an internal current control loop. Therefore, the performance of these systems depends heavily on the current control strategy applied (Kazmierkowski and Malesani 1998).

Several control strategies have been proposed in the literature with the objective of regulating the output currents in three-phase inverters, even though these signals have high harmonic content. In general, these solutions are control structures that have infinite gain in a set of frequencies selected by the designer, being applicable to systems in which it is desired to compensate currents with harmonic components of known orders.

The first modern control strategies for three-phase motor drives required sinusoidal balanced phase currents to be imposed to the machine stator. Due to the widespread use of PI (proportional–integral) controllers, synchronous reference frame (SRF) can be used to transform sinusoidal phase signals into dc quantities, to which PI controllers become adequate (PI-SRF) (Bhattacharya et al. 1996). PI-SRF has been also applied for three-phase grid-connected inverters. Alternatively, the satisfactory results are obtained in stationary reference frame by using the second-order generalized integrator (SOGI) (Zmood and Holmes 2003), also known as resonant controller.

For applications where it is desired to control multiple harmonic components, several works have proposed control schemes whose implementation is carried out in a stationary reference frame, such as multiple SOGIs in parallel (Yuan et al. 2002) and repetitive controllers (RC) (Hara et al. 1988). However, as done for PI-SRF, synchronous references can be used to decrease the number of controllers required (Bojoi et al. 2005). Consequently, these control strategies are sequence-selective at the cost of using rotational transformations (Limongi et al. 2009).

In this scenario, complex controllers can be applied to the space vector generated by three-phase reference signals. In doing so, the designer obtains control schemes that are

✉ Francisco A. S. Neves
fneves@ufpe.br

Rafael C. Neto
rafael.cavalcantineto@ufpe.br

Helber E. P. de Souza
helberelias@pesqueira.ifpe.edu.br

[1] Universidade Federal de Pernambuco, Recife, Brazil

[2] Instituto Federal de Educação Ciência e Tecnologia de Pernambuco, Recife, Brazil

frequency- and sequence-selective, without requiring rotational transformations (Neves et al. 2014).

In this paper, the characteristics and advantages of using space vectors in stationary coordinates as references for control systems are approached. Also, it is demonstrated that real strategies can be decomposed into complex controllers in parallel. Finally, the performances and structure characteristics of real and complex controllers are compared using two different applications. This article is a post-conference paper, which can be seen as a expansion of (Neto et al. 2018a).

2 Space Vectors as Complex References to Control Systems

2.1 Mathematical Basis

Given a set of unbalanced and distorted three-phase periodic signals, it is possible to represent them in *abc* coordinates by the following equations:

$$s_a = \sum_{h=0}^{\infty} s_a^{(h)}; \quad s_b = \sum_{h=0}^{\infty} s_b^{(h)}; \quad s_c = \sum_{h=0}^{\infty} s_c^{(h)}, \tag{1}$$

where s_a, s_b and s_c are instantaneous values of the phase components. The hth harmonic component of phases a, b and c (instantaneous values) can be described by

$$s_i^{(h)} = S_i^{(h)} \cos\left(h\omega_1 t + \varphi_i^{(h)}\right) + S_o^{(h)} \cos\left(h\omega_1 t + \varphi_o^{(h)}\right), \tag{2}$$

for $i = a, b, c$. In this equation, the variables $S_i^{(h)}$, ω_1 and $\varphi_i^{(h)}$ are the amplitude of the harmonic component h, the fundamental frequency and the phase angle of the signal, respectively. The "o" index is used to identify the homopolar component.

As shown in (Neves et al. 2009), when using the Euler expansion in non-homopolar terms, Eq. (2) can be rewritten as

$$\begin{aligned} s_i^{(h)} = {} & S_i^{(h)} \frac{e^{j(h\omega_1 t + \varphi_i^{(h)})} + e^{-j(h\omega_1 t + \varphi_i^{(h)})}}{2} \\ & + S_o^{(h)} \cos\left(h\omega_1 t + \varphi_o^{(h)}\right) \end{aligned} \tag{3}$$

However, since the space vector (Leonhard 1996; Novotny and Lipo 1996) of three-phase signals (evaluated from *abc* reference frame) is calculated by

$$\vec{s}_{\alpha\beta} = \frac{2}{3}\left(s_a + s_b e^{j\frac{2\pi}{3}} + s_c e^{-j\frac{2\pi}{3}}\right), \tag{4}$$

Equation (4) can be used to represent (3) in the $\alpha\beta$ reference frame. In doing so, the homopolar components are eliminated; thus, it becomes

$$\begin{aligned} \vec{s}_{\alpha\beta}^{(h)} = {} & \frac{1}{3} \times \Big[e^{jh\omega_1 t}\left(S_a^{(h)} e^{j\varphi_a^{(h)}} + S_b^{(h)} e^{j\varphi_b^{(h)}} e^{j\frac{2\pi}{3}} \right. \\ & \left. + S_c^{(h)} e^{j\varphi_c^{(h)}} e^{-j\frac{2\pi}{3}}\right) \\ & + e^{-jh\omega_1 t}\left(S_a^{(h)} e^{-j\varphi_a^{(h)}} + S_b^{(h)} e^{-j\varphi_b^{(h)}} e^{j\frac{2\pi}{3}} \right. \\ & \left. + S_c^{(h)} e^{-j\varphi_c^{(h)}} e^{-j\frac{2\pi}{3}}\right) \Big]. \end{aligned} \tag{5}$$

When considering the expansion of complex exponential using Euler formula, and knowing that $\cos(\theta)$ is an even function and $\sin(\theta)$ is an odd function, $e^{-j\theta}$ can be represented by its conjugate (denoted by an asterisk superscript):

$$e^{-j\theta} = (e^{j\theta})^*. \tag{6}$$

Using this property, it is possible to manipulate Eq. (5) in order to obtain

$$\begin{aligned} \vec{s}_{\alpha\beta}^{(h)} = {} & e^{jh\omega_1 t}\left[\frac{1}{3}\left(S_a^{(h)} e^{j\varphi_a^{(h)}} + S_b^{(h)} e^{j\varphi_b^{(h)}} e^{j\frac{2\pi}{3}} \right. \right. \\ & \left. \left. + S_c^{(h)} e^{j\varphi_c^{(h)}} e^{-j\frac{2\pi}{3}}\right)\right] \\ & + e^{-jh\omega_1 t}\left[\frac{1}{3}\left(S_a^{(h)} e^{j\varphi_a^{(h)}} + S_b^{(h)} e^{j\varphi_b^{(h)}} e^{-j\frac{2\pi}{3}} \right. \right. \\ & \left. \left. + S_c^{(h)} e^{j\varphi_c^{(h)}} e^{j\frac{2\pi}{3}}\right)\right]^*. \end{aligned} \tag{7}$$

From this point forward, a phasor representation of the harmonic components will be used to simplify the equations. For this, the reader should consider

$$\tilde{S}_i^{(h)} = S_i^{(h)} e^{j\varphi_i^{(h)}}, \tag{8}$$

for $i = a, b, c$, in which $S_i^{(h)}$ and $\varphi_i^{(h)}$ are the magnitude and phase values of $\tilde{S}_i^{(h)}$, respectively. Thus, by replacing (8) in (7),the following equation is obtained:

$$\begin{aligned} \vec{s}_{\alpha\beta}^{(h)} = {} & e^{jh\omega_1 t}\Bigg[\overbrace{\frac{1}{3}\left(\tilde{S}_a^{(h)} + \tilde{S}_b^{(h)} e^{j\frac{2\pi}{3}} + \tilde{S}_c^{(h)} e^{-j\frac{2\pi}{3}}\right)}^{\tilde{S}_{\alpha\beta+}^{(h)}}\Bigg] \\ & + e^{-jh\omega_1 t}\Bigg[\underbrace{\frac{1}{3}\left(\tilde{S}_a^{(h)} + \tilde{S}_b^{(h)} e^{-j\frac{2\pi}{3}} + \tilde{S}_c^{(h)} e^{j\frac{2\pi}{3}}\right)}_{\tilde{S}_{\alpha\beta-}^{(h)}}\Bigg]^*. \end{aligned} \tag{9}$$

The terms in brackets are the Fortescue's positive- and negative-sequence phasors. It is worth noting that (9) can also be observed as

$$\vec{s}_{\alpha\beta}^{(h)} = \mathrm{e}^{jh\omega_1 t}\tilde{S}_{\alpha\beta+}^{(h)} + \mathrm{e}^{-jh\omega_1 t}\tilde{S}_{\alpha\beta-}^{(h)*}. \tag{10}$$

Therefore, in a generic way, the space vector of any harmonic component of positive- or negative-sequence can be written as

$$\vec{s}_{\alpha\beta}^{(h_\mathrm{s})} = \tilde{S}_{\alpha\beta}^{(h_\mathrm{s})}\mathrm{e}^{jh_\mathrm{s}\omega_1 t}, \tag{11}$$

in which

$$h_\mathrm{s} = \begin{cases} h, & \text{for positive-sequence} \\ -h, & \text{for negative-sequence} \end{cases}. \tag{12}$$

Since $\mathrm{e}^{jh_\mathrm{s}\omega_1 t}$ (for $h_\mathrm{s} \in \mathbb{Z}$) forms an orthogonal basis, it is possible to represent a set of three-phase periodic signals, with no homopolar components, as a sum of harmonic space vectors ($\vec{s}_{\alpha\beta}^{(h_\mathrm{s})}$).

2.2 Harmonic Spectrum of a Space Vector

The Fourier transform can be used to obtain the harmonic spectrum of a space vector (Neves et al. 2009). In this sense, it is calculated by

$$\mathfrak{F}\{\vec{s}_{\alpha\beta}^{(h_\mathrm{s})}\} = \int_{-\infty}^{\infty} \tilde{S}_{\alpha\beta}^{(h_\mathrm{s})}\mathrm{e}^{jh_\mathrm{s}\omega_1 t}\cdot\mathrm{e}^{-j\omega t}dt, \tag{13}$$

but, since $\tilde{S}_{\alpha\beta}^{(h_\mathrm{s})}$ is a constant complex number, it can be rewritten as

$$\mathfrak{F}\{\vec{s}_{\alpha\beta}^{(h_\mathrm{s})}\} = 2\pi\cdot\tilde{S}_{\alpha\beta}^{(h_\mathrm{s})}\cdot\delta(\omega - h_\mathrm{s}\omega_1), \tag{14}$$

where $\delta(\omega - h_\mathrm{s}\omega_1)$ is a unit impulse displaced in $h_\mathrm{s}\omega_1$.

The magnitude and phase plots of the frequency response of a space vector $\vec{s}_{\alpha\beta}^{(h_\mathrm{s})}$ (for a positive-sequence harmonic component h_s) are shown in Fig. 1. From these plots, it is observed that its spectrum does not have symmetry with respect to the ordinate axis. This feature happens because the space vector $\vec{s}_{\alpha\beta}^{(h_\mathrm{s})}$ is represented by a complex signal in the time domain, which implies a complex spectrum as well. Thus, it must be noted that positive frequencies represent positive-sequence harmonic components, while negative frequencies represent negative-sequence harmonic components.

2.3 Space Vectors as References to Control Systems

When considering a system in which a shunt active power filter (SAPF) must compensate the harmonic current required

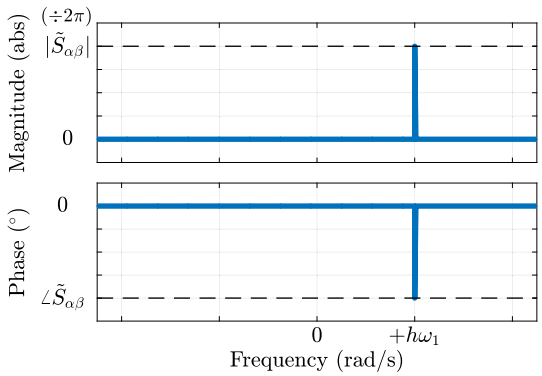

Fig. 1 Frequency response of $\mathfrak{F}\{\vec{s}_{\alpha\beta}^{(h_\mathrm{s})}\}$ for a positive-sequence harmonic component h_s

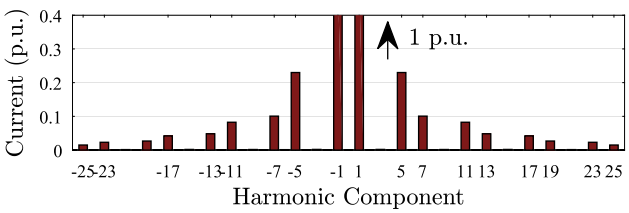

Fig. 2 Harmonic spectrum of the phase-a current of a three-phase diode rectifier

by a three-phase diode rectifier, the abc reference signals have all harmonic components of the family ($6k \pm 1, k \in \mathbb{N}$). In fact, regardless of the grid voltage phase-sequence, the phase currents (i_a, i_b and i_c) will have high harmonic content in the components ($6k \pm 1, k \in \mathbb{N}$), as shown in the harmonic spectrum of phase-a current (Fig. 2).

For the aforementioned application, the currents i_a, i_b and i_c are real signals. As a consequence of this fact, real controllers tuned to obtain high gain in the frequencies ($6k \pm 1$, $k \in \mathbb{N}$) can be applied in abc or $\alpha\beta$ frames to control both positive- and negative-sequence.

However, when using the space vector notation for three-phase signals, it becomes possible to distinguish the harmonic components of positive-sequence from the ones of negative-sequence, as presented in the previous subsection. Figure 3 shows the harmonic spectrum of the space vector obtained from the input currents of the same three-phase rectifier used to plot Fig. 2. In fact, this space vector is calculated by

$$\vec{s}_{\alpha\beta} = \sum_h \vec{s}_{\alpha\beta}^{(h_\mathrm{s})}, \tag{15}$$

in which $h_\mathrm{s} = (6k + 1,\ k \in \mathbb{Z})$, i.e., $h_\mathrm{s} = \{\ldots, -17, -11, -5, +1, +7, +13, +19, \ldots\}$, where the negative signal indicates negative-sequence harmonic components, as can be seen in (12).

In this sense, a complex controller can be applied to the error space vector in three-phase control systems. In doing

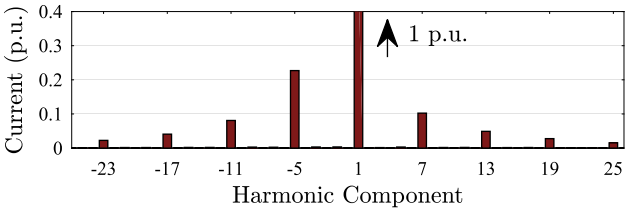

Fig. 3 Harmonic spectrum of the space-vector obtained from the three-phase rectifier input currents

so, the designer obtains a sequence-selective solution that allows to regulate only the required harmonics. In addition, the actual multiple-input and multiple-output (MIMO) control system in a stationary frame can be simplified into a complex single-input and single-output (SISO) system (Luo et al. 2016).

3 Linear Control Strategies for Three-Phase Systems

The main linear control strategies based on the internal model principle for three-phase systems with periodic references or disturbances can be classified in three typical solutions: Integral action in synchronous reference-frame, resonant action and repetitive action. These solutions are briefly described in this section. A three-phase shunt APF is used to exemplify these strategies. As described in Sect. 2.3, in this application, the control system should regulate the current space-vector harmonics of the family $(6k + 1, k \in \mathbb{Z})$ to reduce the harmonic distortion of the grid currents.

3.1 PI Controller in Synchronous Reference-Frame

Even though the PI controller is a simple and widely used solution for systems with constant exogenous signals, this structure does not eliminate the steady-state error for sinusoidal references signals. In order to overcome this issue, the PI controller can be implemented in a synchronous reference frame (Bhattacharya et al. 1996).

Figure 4a shows the block diagram of this control strategy, where the parameter h_s, in the rotational transformation blocks ($\alpha\beta \rightarrow dq$ and $dq \rightarrow \alpha\beta$), indicates the harmonic component and the sequence of phases in which the transformations are tuned. It is worth noting that $\vec{R}(s)$, $\vec{E}(s)$, $\vec{U}(s)$ and $\vec{Y}(s)$ are space vectors, while their indexes indicate whether its reference frame is synchronous (dq) or stationary ($\alpha\beta$).

If the current references are three-phase fundamental frequency and positive sequence (FFPS) signals, the space vector $\vec{e}(t)$ will be constant and the integral action implies zero steady-state error, provided that there are no disturbances with other harmonic components than FFPS. This happens because this control structure has high gain in the harmonic component h_s due to the rotational transformation. Thus, if the reference has other components (or if the voltages in the point of common coupling are not FFPS), the signals in the synchronous reference frame will not be constant and this strategy will not allow reference tracking and disturbances rejection. In fact, a significant error will be seen in the control system, leading to poor performance results, especially in applications with high harmonic content, such as APFs (Buso et al. 1998).

The harmonic spectrum obtained from this controller is not symmetrical with respect to the ordinate axis. Therefore, when using rotational transformations, it becomes possible to use real controllers to obtain a frequency- and sequence-selective control structure. This characteristic, which will be later in this paper linked to complex controllers, is obtained whenever a real controller is used in synchronous reference frame.

Although some authors refer to this strategy as complex vector control, e.g., (Briz et al. 2000), it is actually a real control structure that presents characteristics of a complex controller due to the use of rotational transformations. In fact, it will require higher computational effort than controllers that are already complex without the rotational transformations, here referred as complex controllers.

An alternative solution to contemplate applications with high harmonic content, known as PI-MRI (PI in parallel with multiple rotating integrators), was proposed by (Bojrup et al. 1999). In this strategy, integrators are used in distinct synchronous reference frames, which are tuned for each one of the harmonic components to be compensated. By doing this, each harmonic component will result in constant signals in one of the synchronous reference frames, which makes the integrator adequate for obtaining zero steady-state error (Fig. 4b).

Even though this strategy allows the control system designer to select the harmonic components to be compensated, which is possible due to its modular structure, the PI-MRI controller implies a large computational effort due to the use of multiple rotational transformations (Ghetti et al. 2010).

In fact, $\alpha\beta \rightarrow dq$ transformation can be implemented by

$$\begin{bmatrix} x_d \\ x_q \end{bmatrix} = \begin{bmatrix} \cos(\theta) & \sin(\theta) \\ -\sin(\theta) & \cos(\theta) \end{bmatrix} \begin{bmatrix} x_\alpha \\ x_\beta \end{bmatrix}, \tag{16}$$

while $dq \rightarrow \alpha\beta$ is represented by

$$\begin{bmatrix} x_\alpha \\ x_\beta \end{bmatrix} = \begin{bmatrix} \cos(\theta) & -\sin(\theta) \\ \sin(\theta) & \cos(\theta) \end{bmatrix} \begin{bmatrix} x_d \\ x_q \end{bmatrix}, \tag{17}$$

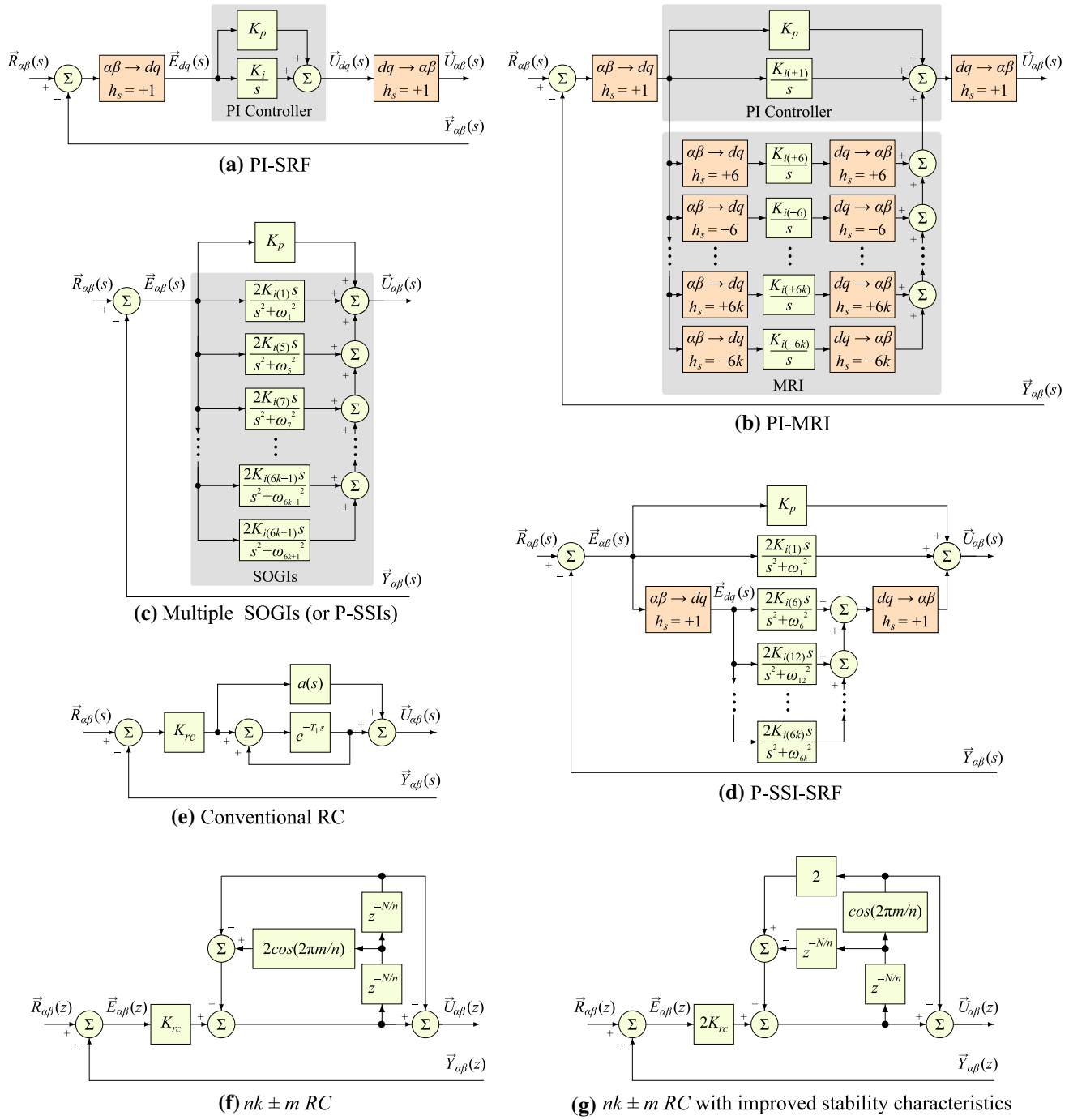

(a) PI-SRF

(b) PI-MRI

(c) Multiple SOGIs (or P-SSIs)

(d) P-SSI-SRF

(e) Conventional RC

(f) $nk \pm m$ *RC*

(g) $nk \pm m$ *RC* with improved stability characteristics

Fig. 4 Block diagram of the control strategies described in Section 3

where θ is usually obtained from a phase locked loop (PLL). Therefore, the rotational transformations used in PI-SRF demand: two trigonometric operations, four sums and eight products. On the other hand, in addition to the two transforms mentioned above, the PI-MRI controller requires $2 \cdot n_{mri}$ transformations, where n_{mri} is the number of rotational integrators to be implemented. When considering only the rotational transformations of the PI-MRI, it demands: $2 + 2 \cdot n_{mri}$ trigonometric operations, $4 + 4 \cdot n_{mri}$ sums and $8 + 8 \cdot n_{mri}$ products. Additional sums and products are required to implement the PI controllers and MRI of these strategies.

3.2 Resonant-Based Controllers

When compared to the structures presented in the previous subsection, this strategy represents a viable solution to reduce the undesirable computational effort from rotational transformations. Since the controllers' transfer function is defined by

$$C_{SOGI}^{(\pm h\omega_1)}(s) = \frac{2K_i s}{s^2 + (h\omega_1)^2}, \tag{18}$$

the resonant action of this second-order generalized integrator (SOGI) presents high gain for $\pm h\omega_1$, ensuring zero steady-state error for sinusoidal references of frequency $h\omega_1$, for both positive- and negative-sequences.

Multiple SOGIs can be used in parallel with a proportional action. When doing so, the poles of each SOGI are allocated to obtain high gain on distinct harmonic components of the exogenous signal to be controlled, as exemplified in Fig. 4c for the control of the family $(6k + 1, k \in \mathbb{Z})$.

It should be noted that if it is only necessary to compensate a single phase-sequence (be it positive or negative), the SOGI will still be designed to control both positive- and negative-sequences, resulting in unnecessary control effort. In other words, even though SOGIs are frequency-selective, they have the same gain for positive- and negative-sequence components of the same order, what means that they are not sequence-selective. The reader should also note that this strategy relies on many generalized integrators to result in good performance when many harmonic components need to be imposed by the controller, which increases the tuning complexity of using multiple SOGIs in parallel.

In order to reduce the number of resonant controllers to be implemented, it is possible to use SOGIs tuned in the harmonics of the family $(6k, k \in \mathbb{Z})$ in a synchronous reference frame, as done for the PI-MRI strategy. In doing so, when evaluating the controllers frequency response in stationary reference frame, the magnitude and phase responses of the SOGIs are shifted to compensate harmonics of the family $(6k + 1, k \in \mathbb{Z})$ (Fig. 5).

Using this idea, Bojoi et al. (2005) proposed the P-SSI-SRF structure (Fig. 4d), which uses a SOGI implemented in the stationary frame to control the FFPS component, while other SOGIs are implemented in a synchronous reference frame to control the other harmonics. Therefore, at the computational cost of two rotational transformations, this strategy makes it possible to compensate for the family $(6k + 1, k \in \mathbb{Z})$ using approximately half of the SOGIs required by the previous strategy (Limongi et al. 2009). The SOGI used to compensate the FFPS component can be replaced by a PI-SRF, as exemplified by (Lascu et al. 2007), whose proposed structure is known as PI-RES.

3.3 Repetitive Controller

Inoue et al. (1981) proposed a controller that presents high gain for a frequency $\omega_L = 2\pi/T_1$, selected by the designer, and for all its harmonics. This strategy, known as repetitive control (RC), consists of using a periodic signal generator as a controller to obtain zero steady-state error for periodic reference signals, what is possible according to the principle of the internal model (Francis and Wonham 1975).

The poles of the periodic signal generator are allocated on the imaginary axis of the complex plane, being spaced by $\omega_L = 2\pi/T_1$. The constant T_1 represents the period of the exogenous signal to be controlled and, consequently, the time delayed by the block $e^{-T_1 s}$ of the RC scheme.

Based on this first work on repetitive control, Hara et al. (1985) proposed a modified scheme (Fig. 4e) that was used as the basis for most of the recent repetitive strategies, which is also known as conventional RC. This modified scheme consists of a periodic signal generator in parallel with a second direct path with gain $a(s)$, which enables to change the zeros allocation. In fact, by selecting a value between 0 and 1 for the parameter $a(s)$, the designer can define the configuration used for implementing the RC. Besides, $a(s)$ influences the stability characteristics of the system, which are improved as $a(s)$ approaches 1 (Hara et al. 1985).

Even though it was simple, the first RC scheme had a major limitation in terms of stability. However, Hara et al. (1985) mathematically demonstrated that this problem could be mitigated by adding a low-pass filter (LPF) to the periodic signal generator. In this scenario, seeking to improve the stability of RC systems while obtaining better frequency selectivity, Mattavelli and Marafao (2004) proposed the use of a RC with highly selective filter for the control of an APF.

The idea of altering the family of harmonic components in which RC applies high gain, used in (Mattavelli and Marafao 2004), can be alternatively implemented by modifying the parameters of RC scheme. In fact, by varying the time delayed by the block $e^{-T_1 s}$ of the RC scheme (T_1) without changing the frequency of the reference signal, the conventional RC compensates a different family of harmonic components, e.g., (Escobar et al. 2006) and (Zhou et al. 2006).

Several studies in the literature present other RC-based solutions for obtaining high gain in harmonic components of a generic family $(nk \pm m, k \in \mathbb{N})$. Most of these solutions use real functions and gains, so these strategies can be implemented using real filters. Examples of these controllers can be found in (Lu and Zhou 2011) and (Neto et al. 2018c) (known as $nk \pm m$ RCs), whose block diagrams are shown in Fig. 4f, g, respectively.

When using any $nk \pm m$ RC in a control system whose reference signals contain only harmonic components of the family $(nk \pm m, k \in \mathbb{N})$, it becomes possible to observe the

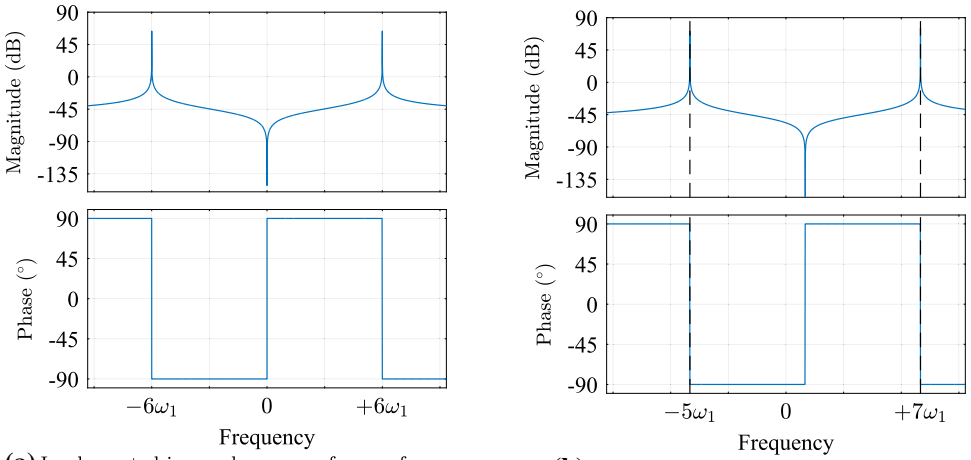

Fig. 5 Effect of the rotational transformations in the frequency response of a SOGI

(a) Implemented in synchronous reference frame.

(b) Referred in stationary reference frame.

advantages of this control structure over conventional RCs. In fact, it provides a reduced-order controller, which stores a smaller number of samples and has faster response than conventional RCs.

4 Complex Controllers Applied to Space Vectors

Although the use of controllers applied to space vectors was initially based on rotational transformations, such as PI-SRF and PI-MRI, this dependency usually results in a undesired computational effort. As consequence, several authors have sought to propose control schemes that did not have these rotational transformations; however, the new schemes should have reduced order when compared to real controllers such as SOGI and RC, while being sequence selective, such as PI-SRF and PI-MRI. The results of such researches, known as complex controllers, are discussed in this section.

A complex controller is characterized by having an asymmetric frequency response with respect to the ordinate axis. Since this aspect is also observed in the space vector notation of three-phase signals (Sect. 2.3), complex controllers are an efficient alternative for this type of application.

According to the internal model principle (Francis and Wonham 1975), if the control system is stable and its open-loop transfer function (OLTF) has a pair of conjugate complex poles located on the imaginary axis in $s = \pm j\omega_1$, the controller guarantees zero steady-state error for tracking sinusoidal references of frequency ω_1. This definition can be extended to complex controllers by considering that a complex pole can be used without its complex conjugate. However, if this controller is applied to space vectors, negative-sequence components are represented as negative harmonic frequencies. Therefore, this class of controllers acts selectively in terms of phase-sequence.

As consequence, these controllers can be classified into: solutions that locate a single imaginary pole, such as the reduced-order generalized integrator (ROGI) (Busada et al. 2012); control schemes that locate more than one imaginary independent pole, such as multiple ROGIs in parallel (Zeng et al. 2014); and controllers that locate multiple poles by applying infinite gain to a periodic set of harmonic components, such as the complex RCs (Luo et al. 2016). In order to select the appropriate control strategy for each application, the designer must evaluate the harmonic spectrum of the space vector that represents the three-phase references.

Three control schemes are reviewed below to illustrate the classes of complex controllers mentioned above.

4.1 ROGI

As proposed in (Busada et al. 2012) and extended in (Zeng et al. 2014), an integrator implemented in a synchronous reference frame can be mathematically described by

$$\vec{U}_{dq}(s) = \vec{E}_{dq}(s) \cdot \frac{K_i}{s}. \tag{19}$$

However, since $\vec{e}_{dq} = \vec{e}_{\alpha\beta} \cdot \mathrm{e}^{-j\omega_0 t}$ and $\vec{u}_{dq} = \vec{u}_{\alpha\beta} \cdot \mathrm{e}^{-j\omega_0 t}$, where ω_0 is the frequency of the reference signals to be controlled (19) can be rewritten as

$$\vec{U}_{\alpha\beta}(s + j\omega_0) = \vec{E}_{\alpha\beta}(s + j\omega_0) \cdot \frac{K_i}{s}. \tag{20}$$

In this way, the ROGI is obtained by making the substitution $s \rightarrow s - j\omega_0$, i.e.,

$$\frac{\vec{U}_{\alpha\beta}(s)}{\vec{E}_{\alpha\beta}(s)} = \vec{C}_{ROGI}^{(+\omega_0)}(s) = \frac{K_i}{s - j\omega_0}, \tag{21}$$

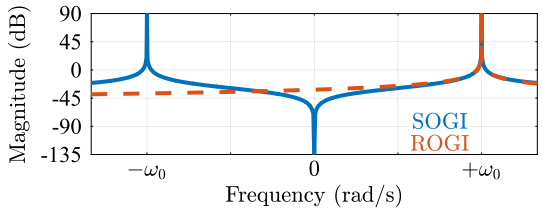

Fig. 6 Magnitude plot of the frequency response of SOGI and ROGI

which applies high gain only at the frequency ω_0. Thus, when applied to a space vector, this ROGI only controls positive-sequence signals of frequency ω_0 (represented as $+\omega_0$).

Alternatively, this transfer function can be obtained from the decomposition of a SOGI into partial fractions (Zeng et al. 2014). In fact, when using two ROGIs with same integral gain in parallel, controlling positive- and negative-sequence harmonic components of same frequency, the obtained control structure is equivalent to a SOGI. That is,

$$C_{SOGI}^{(\pm\omega_0)}(s) = \frac{2K_i s}{s^2+\omega_0^2} = \underbrace{\frac{K_i}{s+j\omega_0}}_{\vec{C}_{ROGI}^{(-\omega_0)}(s)} + \underbrace{\frac{K_i}{s-j\omega_0}}_{\vec{C}_{ROGI}^{(+\omega_0)}(s)}. \tag{22}$$

While the SOGI acts on both positive and negative components, the ROGI controls only one of these. This aspect can be observed by comparing the magnitude plots of the frequency responses of both integrators (Fig. 6). However, it is important to note that if two ROGIs are used in parallel to control the same harmonic components of a SOGI, it is possible to select distinct gains for the compensation of each positive- and negative-sequence component.

This control strategy in discrete-time applications requires the compensation of the computational delay, since it can make the control system unstable. Thus, a discrete-time ROGI with phase compensation was proposed in (Xie et al. 2017), whose transfer function is

$$\vec{C}_{ROGI}^{(+\omega_0)}(z) = K_i T_s \cdot \frac{z \cdot e^{-j\phi_h}}{z - e^{jh\omega_0 T_s}}, \tag{23}$$

in which T_s is the sampling period, h is the controlled harmonic component and ϕ_h is the phase lead angle. Besides that, a proportional action is usually added in parallel with the ROGI to allow the selection of the control system bandwidth.

Other control strategies that also implement the complex resonant action were proposed in the literature. Two examples are: the controller based on the space vector Fourier transform (Neves et al. 2014) and the PI-SRF, which was presented in the previous section.

In applications where many harmonic components must be controlled, multiple ROGIs can be used in parallel with a single proportional gain. However, since applying a high gain to high harmonic components may turn the system unstable, high-frequency ROGIs (and SOGIs) should have lower gains than the low-frequency ones. Figure 7 shows the block diagram of this control scheme.

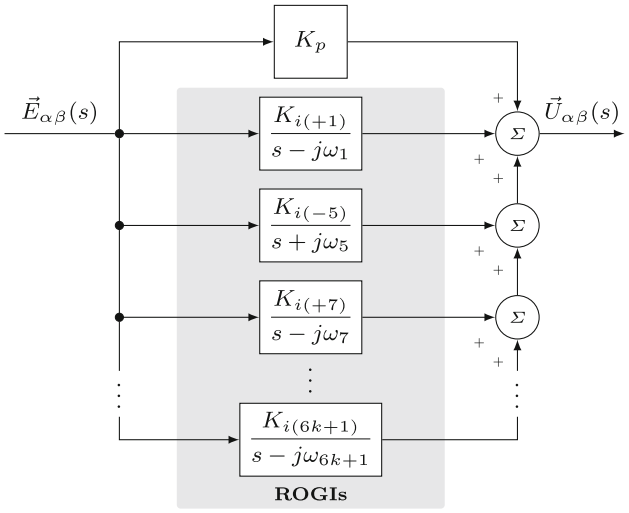

Fig. 7 Control structure based on multiple ROGIs in parallel

4.2 Complex RC

After evaluating the harmonic spectrum of the reference space vector, if the control system designer realizes that it is necessary to control the harmonic components of a periodic family, such as $(nk+m, k \in \mathbb{Z})$, the satisfactory results can be obtained by using a complex RC applied to the error space vector (Luo et al. 2016). In fact, when compared to multiple ROGIs in parallel, complex RCs are simpler to implement and design.

The solution proposed in (Zimann et al. 2019) has the following transfer function:

$$\vec{C}_{RC}^{(nk+m)}(z) = \frac{1}{\vec{a}} \cdot \frac{K_{rc}}{1 - e^{j2\pi\frac{m}{n}} \cdot z^{-\frac{N}{n}}}, \tag{24}$$

where $n > m \geq 0$, N is the number of samples per fundamental period and $\vec{a}$ is a constant complex gain. The block diagram of this complex controller is shown in Fig. 8. The magnitude plot of the frequency response of this controller is shown in Fig. 9.

Since this control structure is based on the conventional RC (Hara et al. 1988), a finite impulse response (FIR) filter can be used in cascade with the delay of the periodic signal generator ($z^{-\frac{N}{n}}$) in order to increase the system's relative stability. This is done because, when applying a high gain to high harmonic components, the system may become unstable.

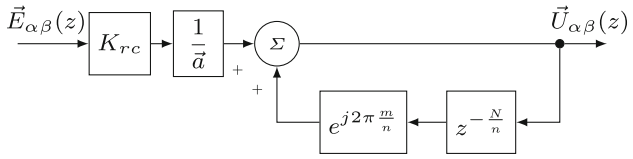

Fig. 8 Block diagram of complex $nk + m$ RC proposed by (Zimann et al. 2019)

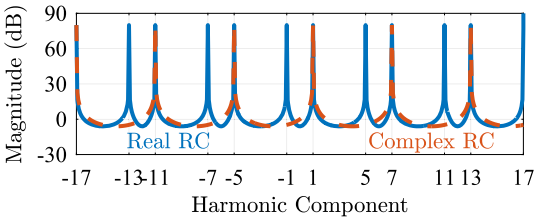

Fig. 9 Magnitude plots of the complex RC proposed by (Zimann et al. 2019) and real RC proposed by (Neto et al. 2018c) to control the families ($6k + 1$, $k \in \mathbb{Z}$) and ($6k \pm 1$, $k \in \mathbb{N}$), respectively

There are several proposals in the literature of real RCs that can control the generic family ($nk \pm m$, $k \in \mathbb{N}$), e.g., the schemes in Fig. 4f, g. As done for the ROGI, complex RCs can be obtained by decomposing a real $nk \pm m$ RC into complex RCs that control the components $nk+m$ and $nk-m$ separately.

In fact, by decomposing the $nk \pm m$ RC proposed in (Neto et al. 2018c), whose block diagram is shown in Fig. 4g and transfer function is calculated by

$$C_{RC}^{(nk\pm m)}(z) = \frac{K_{rc} \cdot \left[1 - z^{-\frac{N}{n}} \cdot \cos\left(2\pi\frac{m}{n}\right)\right]}{1 - z^{-\frac{N}{n}} \cdot 2 \cdot \cos\left(2\pi\frac{m}{n}\right) + z^{-2\frac{N}{n}}}, \tag{25}$$

the following equation is obtained

$$C_{RC}^{(nk\pm m)}(z) = \frac{K_{rc}}{2} \cdot \underbrace{\frac{1}{1 - \mathrm{e}^{j2\pi\frac{m}{n}} \cdot z^{-\frac{N}{n}}}}_{\vec{C}_{RC}^{(nk+m)}(z) \text{ for } \vec{a}=1} + \frac{K_{rc}}{2} \cdot \underbrace{\frac{1}{1 - \mathrm{e}^{-j2\pi\frac{m}{n}} \cdot z^{-\frac{N}{n}}}}_{\vec{C}_{RC}^{(nk-m)}(z) \text{ for } \vec{a}=1}. \tag{26}$$

This feature can also be observed in the complex controller proposed by (Luo et al. 2016) (Fig. 10), which can be obtained from the decomposition of the real $nk \pm m$ RC proposed in (Lu and Zhou 2011) (Fig. 4f).

As in previous strategies, the effect of computational delay must be compensated. A simple way to mitigate it can be achieved by using a phase lead cascaded with the repetitive controller (Neto et al. 2018b).

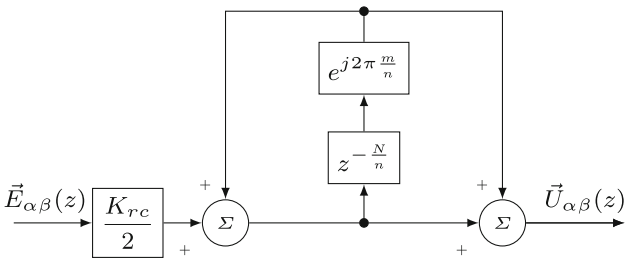

Fig. 10 Block diagram of complex $nk + m$ RC proposed by (Luo et al. 2016)

4.3 Bibliographic Review Analysis

After describing the main real and complex control strategies based on the internal model principle, it becomes possible to evaluate the chronological development of these schemes when applied to inverters through a timeline (Fig. 11).

As can be seen in Fig. 11, for a long time only PI-SRFs were used for controlling inverters. This stems from the fact that most of control strategies for electric motors are implemented in synchronous reference frame. Besides, in these applications, the reference signals usually have only the FFPS component; however, the frequency may vary, what makes the use of a synchronous reference frame useful.

When considering the real control strategies applied to APFs, whose reference signals have several harmonic components, it is observed that most of the evaluated papers are dated in the 1990s and 2000s. When evaluating complex control strategies (schemes without rotational transformations), the first controller applied to electrical systems was proposed in 2012 (ROGI), while the first application of generic-order complex RC ($nk + m$ RC) is dated 2016. Finally, complex control strategies applied to electrical systems represent a very recent field of research; therefore, their common characteristics should be properly studied.

5 Characteristics of Complex Controllers

5.1 Coupling Between the α and β Stationary Axes

The real and imaginary parts of a complex gain operation can be represented through a matrix as follows:

$$\vec{Y}_{\alpha\beta} = (a + jb) \cdot \vec{X}_{\alpha\beta} \equiv \begin{bmatrix} Y_\alpha \\ Y_\beta \end{bmatrix} = \begin{bmatrix} a & -b \\ b & a \end{bmatrix} \cdot \begin{bmatrix} X_\alpha \\ X_\beta \end{bmatrix}, \tag{27}$$

then, when manipulating the transfer function of a complex controller in order to obtain a scalar implementation structure, all complex poles, zeros and gains result in a coupling between the α and β stationary axes.

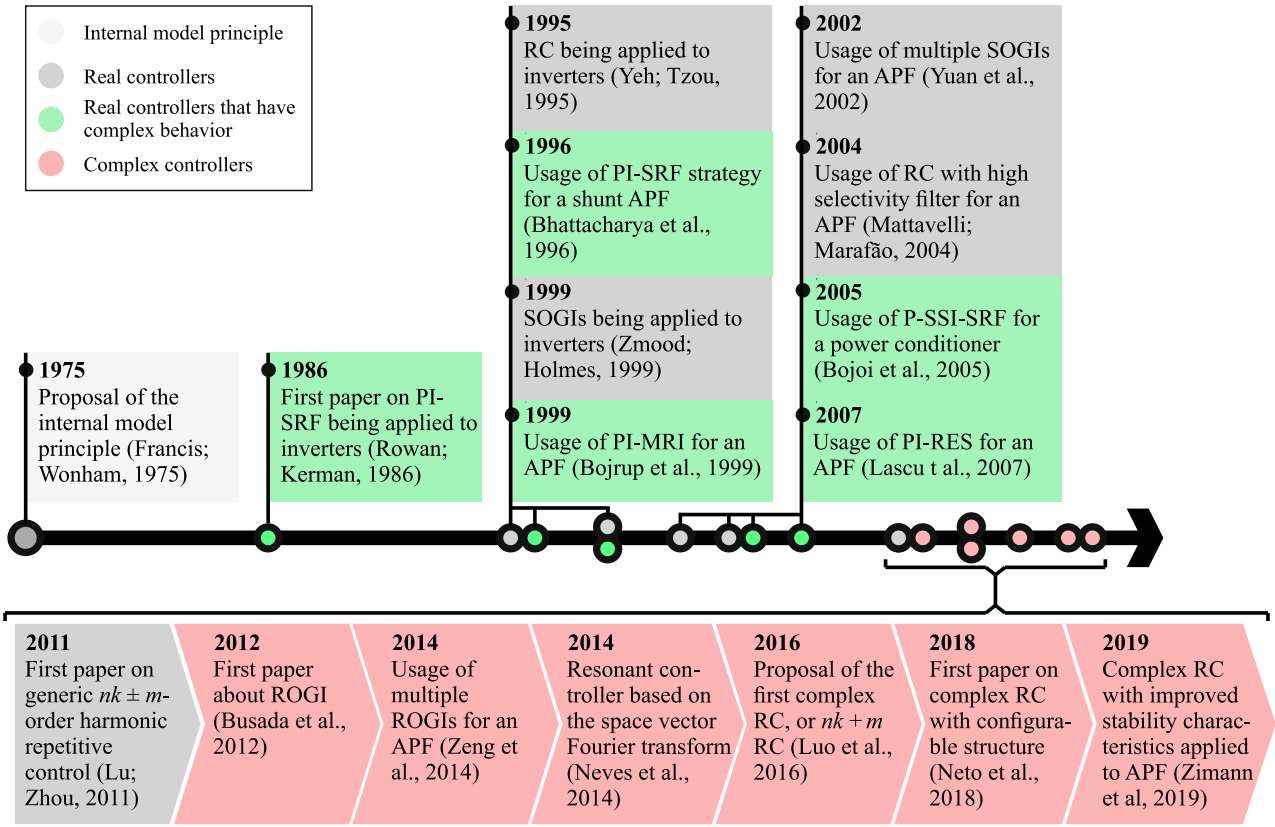

Fig. 11 Timeline presenting relevant publications related to real and complex control structures based on the internal model principle

Taking a ROGI as example (21) can be rewritten as

$$\begin{aligned} \vec{U}_{\alpha\beta}(s) \cdot (s - j\omega_0) &= \vec{E}_{\alpha\beta}(s) \cdot K_i, \\ \vec{U}_{\alpha\beta}(s) \cdot s &= \vec{E}_{\alpha\beta}(s) \cdot K_i + \vec{U}_{\alpha\beta}(s) \cdot j\omega_0. \end{aligned} \tag{28}$$

Thus, using matrix notation, it leads to

$$\begin{bmatrix} U_\alpha(s) \\ U_\beta(s) \end{bmatrix} \cdot s = \begin{bmatrix} E_\alpha(s) \\ E_\beta(s) \end{bmatrix} \cdot K_i + \begin{bmatrix} U_\alpha(s) \\ U_\beta(s) \end{bmatrix} \cdot \begin{bmatrix} 0 & -\omega_0 \\ \omega_0 & 0 \end{bmatrix},$$

i.e.,

$$\begin{cases} U_\alpha(s) = 1/s \cdot \left[E_\alpha(s) \cdot K_i - U_\beta(s) \cdot \omega_0\right] \\ U_\beta(s) = 1/s \cdot \left[E_\beta(s) \cdot K_i + U_\alpha(s) \cdot \omega_0\right] \end{cases}. \tag{29}$$

In other words, $U_\alpha(s)$ depends on $U_\beta(s)$ and vice versa. This same characteristic can be seen in the complex RCs proposed in (Luo et al. 2016) and (Zimann et al. 2019).

However, when considering a space vector notation, complex controllers are designed considering a complex SISO system. The influence of the coupling between the α and β axes interferes positively the control system, as will be discussed in Sect. 5.3. The implementation in digital signal processors (DSP) still depends on a MIMO representation, as shown in (29). It should be noted that real controllers with complex behavior, e.g., PI-SRF and PI-MRI, have their coupling implemented in their rotational transformations.

5.2 Stability Analysis for Both Positive and Negative Spectra

In order to analyze the stability of complex control systems, the designer must evaluate both positive and negative spectra separately and adopt the worst of them. This condition arises from the fact that each of these frequency bands has a different frequency response (Shen et al. 2012). This fact is evidenced by the lack of symmetry when evaluating the Nyquist diagram of complex control systems' OLTF ($T(z)$), as exemplified in Fig. 12 for a hypothetical plant with damped-ROGI (ROGI with a small real part at its pole).

In this sense, the control system will be stable only if both its positive and negative spectra point to the absolute stability of the system. As for the relative stability, one should evaluate the phase and gain margins (PM and GM) separately for the positive spectrum (PM_+ and GM_+) and negative spectrum (PM_- and GM_-). Then, the following values are set as the phase and gain margins of the complex system:

$$\begin{aligned} PM &= \min(PM_+, PM_-) \\ GM &= \min(GM_+, GM_-) \end{aligned}, \tag{30}$$

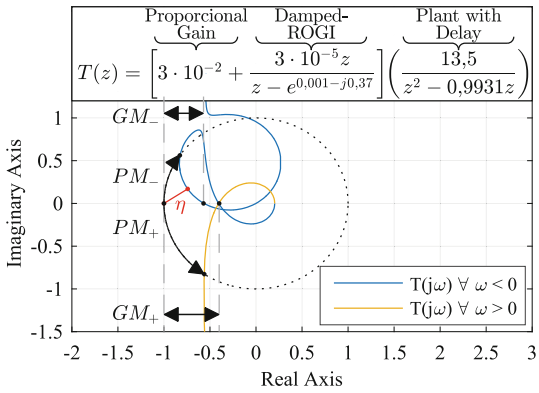

Fig. 12 Nyquist diagram of the OLTF $T(z)$ for a hypothetical minimum phase complex control system

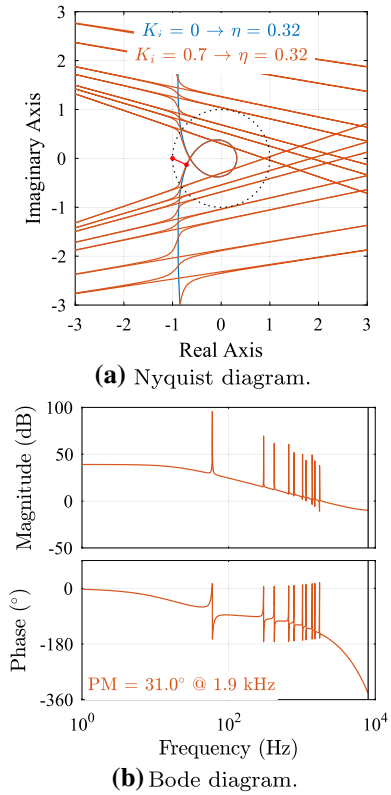

(a) Nyquist diagram.

(b) Bode diagram.

Fig. 13 Nyquist and bode diagrams of the OLTF of a system with multiple SOGIs. Diagrams obtained for $K_i = 0.7$

in which $\min(A_1, A_2)$ denotes the lowest value among A_1 and A_2. For the example shown in Fig. 12, the phase and gain margins are $PM = PM_-$ and $GM = GM_-$.

The relative stability can be evaluated for the entire frequency spectrum, in a single step, by evaluating the systems' sensitivity function (Yepes et al. 2011). This stability indicator is shown in Fig. 12 as η, and it represents the minimum distance between the Nyquist diagram of the OLTF and the critical point $(-1, 0)$.

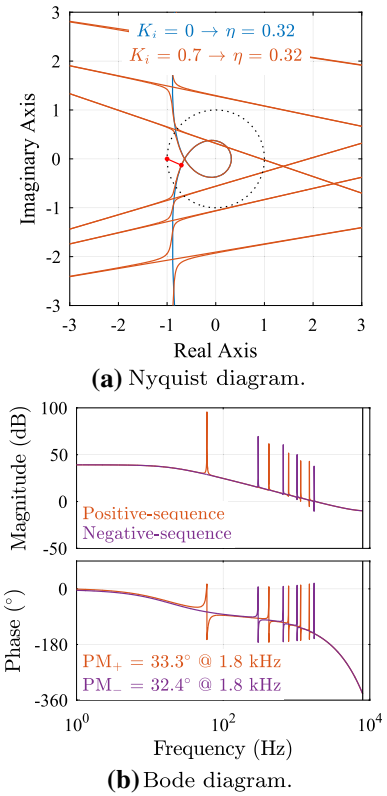

(a) Nyquist diagram.

(b) Bode diagram.

Fig. 14 Nyquist and bode diagrams of the OLTF of a system with multiple ROGIs. Diagrams obtained for $K_i = 0.7$

5.3 Lower Order and Better Stability Characteristics

When it is desired to control three-phase references that have different harmonic components of distinct sequences, e.g., $h_s = \{-11, -5, +1, +7, +13\}$, the use of complex controllers applied to space vectors reduces by up to two times the order of the control scheme. For these situations, including a real controller in the stationary reference frame does not entail additional performance benefits but increases the controller's order.

In fact, if it is necessary to control a vector reference that has only the fundamental frequency- and positive-sequence (FFPS) component $h_s = \{+1\}$, the satisfactory results are obtained using only one ROGI. Thus, if a SOGI is used for this same application, the control structure has its order increased unnecessarily.

If the reference contains all harmonics of a family $(nk + m, k \in \mathbb{Z})$, $2 \cdot N/n$ memory cells are required in order to implement the $nk + m$ RC proposed by (Zimann et al. 2019), and the controller will have order N/n. Meanwhile, $2 \cdot N/n$ memory cells per stationary axis are required to implement the $nk \pm m$ RC proposed by (Neto et al. 2018c) (i.e., a total of $4 \cdot N/n$ for $\alpha\beta$ reference frame), leading to a scheme of order $2 \cdot N/n$.

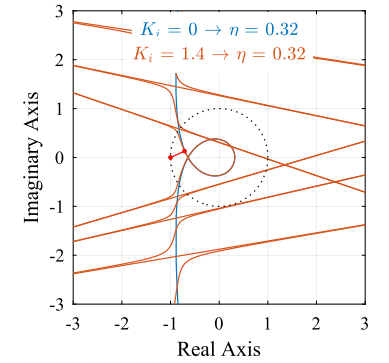

(a) Nyquist diagram.

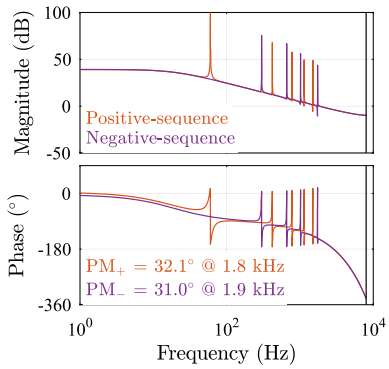

(b) Bode diagram.

Fig. 15 Nyquist and bode diagrams of the OLTF of a system with multiple ROGIs. Diagrams obtained for $K_i = 1.4$

In applications where the set of harmonics to be controlled do not include positive- and negative-sequence components of the same order, e.g., $h_a = \{-29, -23, -17, -11, -5, +1, +7, +13, +19, +25\}$, the use of complex controllers reduces the number of harmonic components in which the control scheme applies high gain, resulting in better stability characteristics.

In order to illustrate this feature, let us consider that the output current of a three-phase shunt APF with the first-order output filter must be controlled, which can be modeled as

$$G_p(s) = \frac{\frac{V_{dc}}{R_f}}{1 + \frac{L_f}{R_f}s}, \tag{31}$$

where $V_{dc} = 600\,\text{V}$, $L_f = 2.56\,\text{mH}$ and $R_f = 307.5\,\text{m}\Omega$. Then, in space vector notation, the set of harmonics used as example above (h_a) must be compensated for obtaining grid currents with low THD. In this scenario, if the control system designer chooses multiple SOGIs as control scheme to be implemented, the OLTF will present high gain in the harmonics:

$$h_{SOGIs} = \{-29, -25, -23, -19, -17, -13, -11, -7, -5, -1, +1, +5, +7, +11, +13, +17, +19, +23, +25, +29\},$$

leading to the Nyquist diagram shown in Fig. 13a, which presents a phase margin of 31.1° (Fig. 13b). The same resonant gain K_i was used for all SOGIs, regardless of the frequency they are tuned. On the other hand, if multiple ROGIs are chosen as control scheme, the OLTF will have high gain in the harmonics:

$$h_{ROGIs} = \{-29, -23, -17, -11, -5, +1, +7, +13, +19, +25\},$$

leading to the Nyquist diagram shown in Fig. 14a, which presents a phase margin of 32.4° (Fig. 14b). The same resonant gain K_i was used for all ROGIs, regardless of the frequency they are tuned.

This improvement in system stability is resulted from the fact that the resonance peaks applied by the complex control scheme are better distributed in the positive and negative spectra. As they are more spaced from each other, their impacts on system stability will be reduced, which will be especially beneficial for high-frequency harmonics. In fact, the system with complex controllers will have better stability characteristics if multiple harmonic components around the 0 dB gain crossing frequency must be controlled, as exemplified in Figs. 13 and 14.

The gain of complex controllers can be increased to make their stability indicators and 0dB gain crossing frequency similar to those obtained when real controllers are used, as can be seen when comparing Figs. 13 and 15. As consequence, since the controllers' gain increases, better results of settling time and total harmonic distortion are expected, which will be confirmed in the experimental results (Sect. 6).

5.4 Implementation Issues

As discussed in Sect. 5.1, the use of complex controllers implies the coupling between α and β axes. This feature can be evidenced when evaluating how these controllers are implemented in a DSP, as can be seen in Figs. 16, 17 and 18.

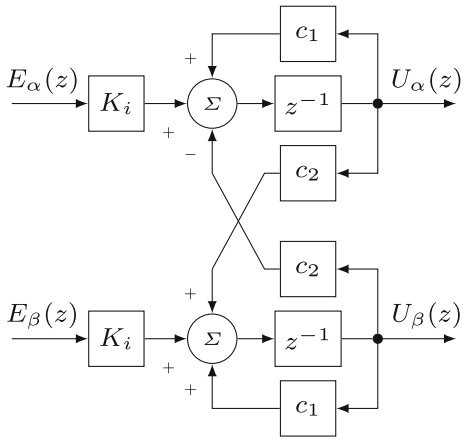

Fig. 16 Implementation of the ROGI as proposed by (Busada et al. 2012), where $c_1 = \cos(h\omega_1 T_s)$ and $c_2 = \sin(h\omega_1 T_s)$

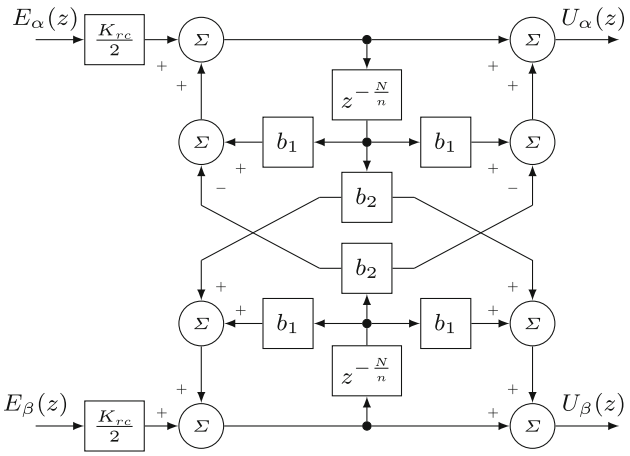

Fig. 17 Implementation of the complex $nk + m$ RC proposed by (Luo et al. 2016), where $b_1 = \cos(2\pi \frac{m}{n})$ and $b_2 = \sin(2\pi \frac{m}{n})$

When designing these controllers, the computational delay of the digital implementation must be taken into account. To work around this issue, two solutions can be used: For multiple ROGIs, a phase compensation must be implemented for each ROGI separately (Xie et al. 2017), as indicated in (23); for complex RCs, a lead compensator should be cascaded with the controller, as proposed in (Zimann et al. 2019).

5.5 Structural Comparison Between Real and Complex Controllers

Table 1 is filled in with the main structural characteristics of each controller presented in this paper. The characteristics considered in this comparison are: (i) total number of memory cells used to implement each control scheme; (ii) target application, which indicates the harmonics and phase-sequences the controller is able to synthesize; (iii) if the control scheme implies a coupling between stationary axes; and (iv) the total number of sums, products and trigonometric

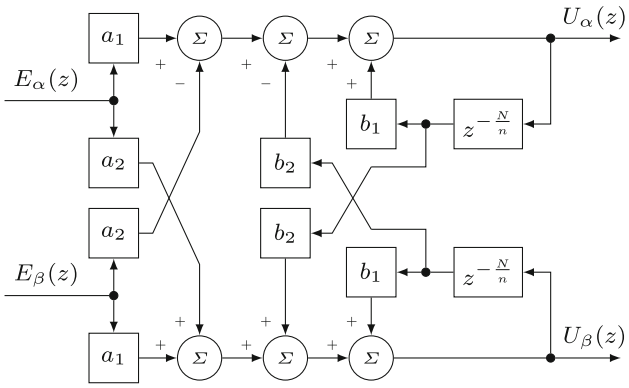

Fig. 18 Implementation of the complex $nk + m$ RC proposed by (Zimann et al. 2019), where $a_1 = K_{rc} \cdot real(\vec{a}^{-1})$, $a_2 = K_{rc} \cdot imag(\vec{a}^{-1})$, $b_1 = \cos(2\pi \frac{m}{n})$ and $b_2 = \sin(2\pi \frac{m}{n})$

operations used to implement each controller (computational cost).

The data related to computational cost were computed considering the following factors:

- SOGIs being discretized through Tustin method, as presented in (Rodriguez et al. 2008);
- Discrete-time integrators (used in PI-SRF and PI-MRI) being implemented through forward Euler method;
- Complex controllers being implemented as indicated in Figs. 16, 17 and 18);
- Real RCs being implemented as their block diagrams are in Fig. 4;
- n_{rogi} is the number of ROGIs used in P + Multiple ROGIs scheme;
- n_{sogi} is the number of SOGIs used in P + Multiple SOGIs and P-SSI-SRF schemes;
- n_{mri} is the number of rotating integrators used in PI-MRI scheme;
- The parameter N (in RC control schemes) is the number of samples per fundamental period.

The computational cost of $abc \rightarrow \alpha\beta$ and $\alpha\beta \rightarrow abc$ transformations is not computed in Table 1. However, since PI-SRF, PI-MRI and P-SSI-SRF schemes require rotational transformations, the computational cost of such operations is taken into account.

From Table 1, it can be seen that:

- When only one phase-sequence must be controlled, the use of complex controllers requires fewer memory cells than real controllers. For instance, for controlling a single harmonic in $\alpha\beta$ reference frame, P + ROGI scheme requires two memory cells while P + SOGI scheme requires eight memory cells;

Table 1 Summary of the structural similarities and differences between the control schemes presented in Sects. 3 and 4

Control scheme	Total number of memory cells	Target application**	Coupling between stationary axes	Number of sums and products
Real controllers				
P + SOGI (Zmood and Holmes 1999)	$4 \cdot NoA^*$	A single harmonic (both sequences)	No	$sums \rightarrow 6 \cdot NoA^*$ $prod. \rightarrow 3 \cdot NoA^*$
P + Multiple SOGIs (Yuan et al. 2002)	$4 \cdot n_{sogi} \cdot NoA^*$	Multiple harmonics (both sequences)	No	$sums \rightarrow (6 \cdot n_{sogi}) \cdot NoA^*$ $prod. \rightarrow (1 + 2 \cdot n_{sogi}) \cdot NoA^*$
Conventional RC (Hara et al. 1988)	$N \cdot NoA^*$	All harmonics (both sequences)	No	$sums \rightarrow 2 \cdot NoA^*$ $prod. \rightarrow 2 \cdot NoA^*$
$nk \pm m$ RC (Lu and Zhou 2011)	$2 \cdot \frac{N}{n} \cdot NoA^*$	$h =(nk \pm m, k \in \mathbb{N})$ (both sequences of each h)	No	$sums \rightarrow 3 \cdot NoA^*$ $prod. \rightarrow 2 \cdot NoA^*$
$nk \pm m$ RC (Neto et al. 2018c)	$2 \cdot \frac{N}{n} \cdot NoA^*$	$h =(nk \pm m, k \in \mathbb{N})$ (both sequences of each h)	No	$sums \rightarrow 3 \cdot NoA^*$ $prod. \rightarrow 3 \cdot NoA^*$
Control scheme	Total number of memory cells	Target application**	Coupling between stationary axes	Number of sums, products and trigo-nometric operations
*Real controllers that have complex behavior***				
PI-SRF (Bhattacharya et al. 1996)	4	A single harmonic (one sequence)	Yes (in Park transf.)	$sums \rightarrow 8$ $prod. \rightarrow 12$ $trig. \rightarrow 2$
PI-MRI (Bojrup et al. 1999)	$4 + 4 \cdot n_{mri}$	Multiple harmonics (one sequence for each rotating integrator)	Yes (in Park transf.)	$sums \rightarrow 8 + 8 \cdot n_{mri}$ $prod. \rightarrow 12 + 10 \cdot n_{mri}$ $trig. \rightarrow 2 + 2 \cdot n_{mri}$
P-SSI-SRF (Bojoi et al. 2005)	$8 \cdot n_{sogi}$	Multiple harmonics (fund.: both sequence; others: one sequence)	Yes (in Park transf.)	$sums \rightarrow 4 + 12 \cdot n_{sogi}$ $prod. \rightarrow 10 + 4 \cdot n_{sogi}$ $trig. \rightarrow 2$
Control scheme	Total number of memory cells	Target application**	Coupling between stationary axes	Number of sums and products
Complex controllers				
P + ROGI (Busada et al. 2012)	2	A single harmonic (one sequence)	Yes (in the controller)	$sums \rightarrow 6$ $prod. \rightarrow 8$
P + Multiple ROGIs (Zeng et al. 2014)	$2 \cdot n_{rogi}$	Multiple harmonics (one sequence each)	Yes (in the controller)	$sums \rightarrow 6 \cdot n_{rogi}$ $prod. \rightarrow 2 + 6 \cdot n_{rogi}$
$nk + m$ RC (Luo et al. 2016)	$2 \cdot \frac{N}{n}$	$h_s =(nk + m, k \in \mathbb{N})$ (one sequence for each h_s)	Yes (in the controller)	$sums \rightarrow 8$ $prod. \rightarrow 8$
$nk + m$ RC (Zimann et al. 2019)	$2 \cdot \frac{N}{n}$	$h_s =(nk + m, k \in \mathbb{N})$ (one sequence for each h_s)	Yes (in the controller)	$sums \rightarrow 6$ $prod. \rightarrow 8$

*$NoA = 3$ for implementation using abc reference frame; $NoA = 2$ for implementation using $\alpha\beta$ reference frame
**Both sequences → Scheme controls BOTH positive- and negative-sequences
One sequence → Scheme controls only positive-sequence OR negative-sequence, but not both

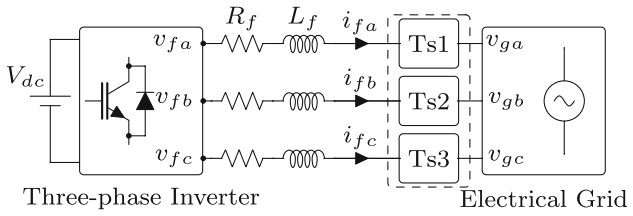

Fig. 19 Block diagram of Application 1

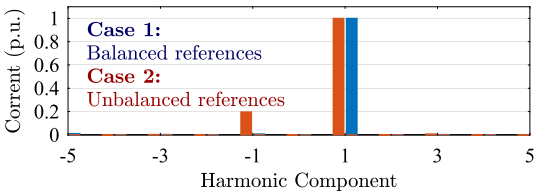

Fig. 20 Harmonic spectrum of the reference space vector ($\vec{i}_f^*$), with and without unbalance

– RC-based controllers demand fewer sums and products than using multiple SOGIs or ROGIs. However, a higher total number of memory cells are required;
– Even though real controllers implemented in synchronous reference frame have complex behavior, the computational cost of the rotational transformations makes this class of controllers to have the worst characteristics in terms of number of sums, products and trigonometric operations. For this reason, this control strategy was not included in the experimental comparison.

6 Experimental Results

Two applications were used to obtain the experimental results and evaluate complex controllers. All control strategies evaluated below were implemented in dSPACE, model DS1005, with 1 GHz processor.

6.1 Application 1: Active Power Injection in a Three-Phase Grid

Figure 19 shows the block diagram of Application 1, while Table 2 displays the parameters of the prototype. Blocks Ts1, Ts2 and Ts3 represent single-phase transformers used in Y-Y for connecting the inverter to the electrical grid, with turns ratio of N_{Ts} and leakage inductance of L_{Ts}. For the experimental results, the sampling and switching frequency f_s, and fundamental frequency f_1 were used. The evaluated controllers were used in a current control loop so that it was possible to control the variables i_{fa}, i_{fb} and i_{fc}.

Initially, both ROGI and SOGI were used together with a proportional (P) action to impose a constant active power injection into a three-phase balanced grid. As consequence,

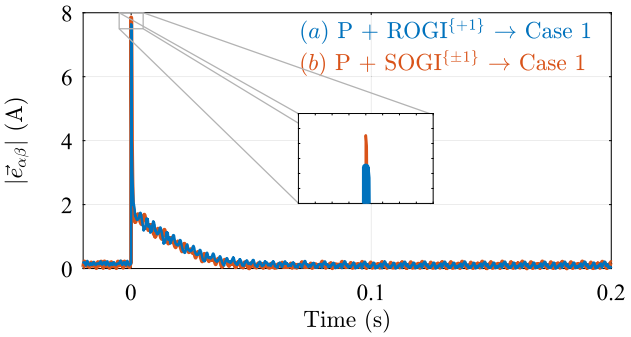

Fig. 21 Magnitude error of the controllers evaluated in Application 1 ($|\vec{e}_{\alpha\beta}|$) for balanced references (Case 1). Transient evaluated for step magnitude variation of 1 p.u. in the reference currents

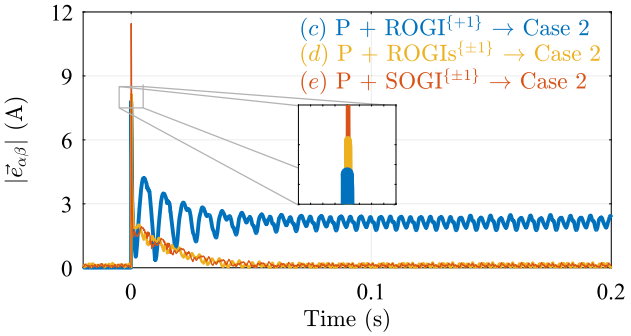

Fig. 22 Magnitude error of the controllers evaluated in Application 1 ($|\vec{e}_{\alpha\beta}|$) for unbalanced references (Case 2). Transient evaluated for step magnitude variation of 1 p.u. in the reference currents

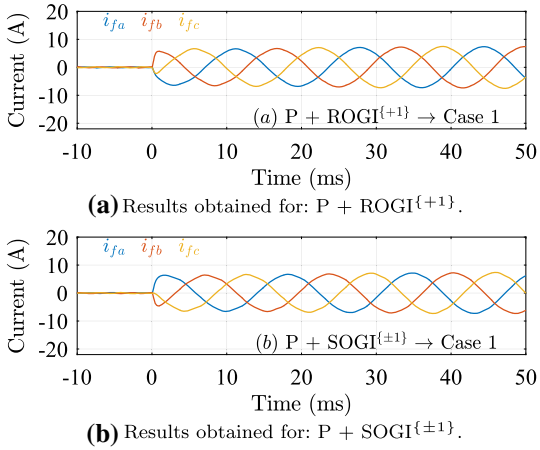

Fig. 23 Inverter output currents of the controllers evaluated in Application 1 for balanced references (Case 1). Results obtained using dSPACE platform

the reference space vector had only the FFPS component (Fig. 20) and the following control schemes were implemented: (a) P + ROGI$^{\{+1\}}$, tuned in $h_s = \{+1\}$; and (b) P + SOGI$^{\{\pm1\}}$.

Then, the turns ratio of transformer Ts3 was changed to simulate an unbalance in the mains voltages. Thus, the

Table 2 Parameters of the prototypes used for Applications 1 and 2

Common to both applications				Application 1						Application 2							
L_f (mH)	R_f (mΩ)	f_s* (kHz)	f_1** (Hz)	V_{dc} (V)	$V_{g(line)}$ (V_{rms})	K_p	K_i	N_{Ts}	L_{Ts} (mH)	V_{dc} (V)	$V_{g(line)}$ (V_{rms})	$\frac{N}{n}$	$\frac{M}{2}$	R_g (mΩ)	L_g (μH)	L_l (mH)	R_l (Ω)
2.56	307.5	17.28	60	500	220	0.0125	0.3	1:1	1.48	600	380	48	3	31.7	186.2	1.48	48.5

* $f_s \rightarrow$ Sampling and switching frequency
** $f_1 \rightarrow$ Grid frequency
$f_s/f_1 = N$ must be integer and f_s must be multiple of 32 because of the PLL used in ref. generation (Neves et al. 2010)

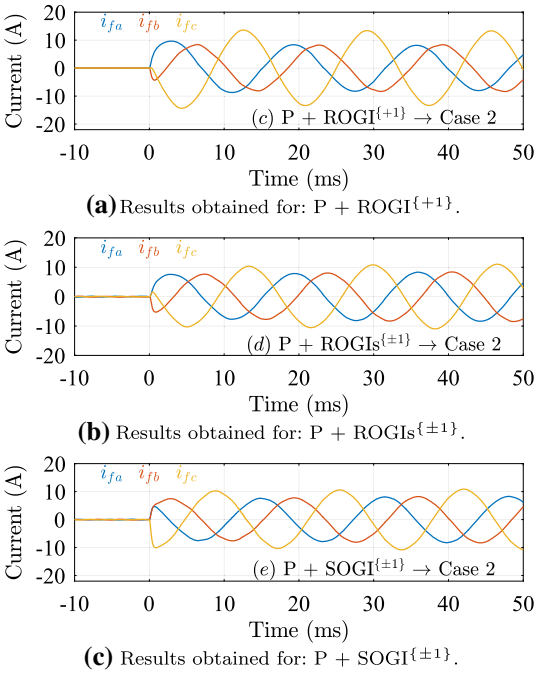

(a) Results obtained for: P + ROGI$^{\{+1\}}$.

(b) Results obtained for: P + ROGIs$^{\{\pm 1\}}$.

(c) Results obtained for: P + SOGI$^{\{\pm 1\}}$.

Fig. 24 Inverter output currents of the controllers evaluated in Application 1 for unbalanced references (Case 2). Results obtained using dSPACE platform

reference space vector ($\vec{i}_f^*$) will now need high gain in the components $h_s = \{-1; +1\}$ (Fig. 20). For this new configuration, the performance of the following controllers were evaluated: (*c*) P + ROGI$^{\{+1\}}$, tuned in $h_s = \{+1\}$; (*d*) P + ROGIs$^{\{\pm 1\}}$, tuned in the components $h_s = \{-1; +1\}$; and (*e*) P + SOGI$^{\{\pm 1\}}$.

All strategies were implemented using the same proportional and integral gains. In addition, both ROGI and SOGI were discretized using the "Tustin with pre-warping" method, in order to ensure that the high gain peaks will be at the desired frequencies for the discrete-time system (Yepes et al. 2010). The stability evaluation and the controllers tuning were done using the sensitivity index (Yepes et al. 2011). In order to mitigate the effect of the computational delay, both SOGI and ROGI were implemented with phase compensation, as suggested in (Yepes et al. 2011) and (Xie et al. 2017), respectively. The magnitude error for each evaluated controller is shown in Fig. 21 (for balanced references) and Fig. 22 (for unbalanced references). The inverter output current for each evaluated controller is shown in Fig. 23 (for balanced references) and Fig. 24 (for unbalanced references).

For the results (a) and (d), the ROGIs are tuned to the harmonic components whose harmonic spectrum of the reference space vector presents high harmonic content. Thus, it has obtained a similar performance to that obtained with SOGIs in (b) and (e); however, the controller used for (a) has lower order. For the result (c), since the reference signal has harmonic content in the components $h_s = \{-1; +1\}$ but

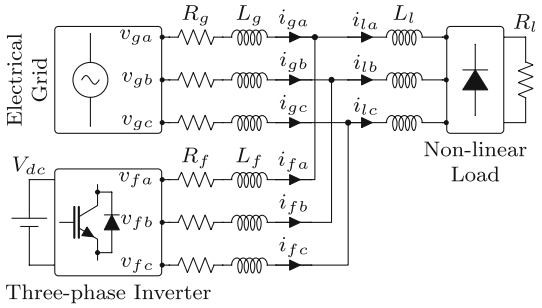

Fig. 25 Block diagram of Application 2

only one ROGI tuned to $h_s = \{+1\}$ was implemented, it was not possible to eliminate the steady-state error.

In conclusion, since the same gains were used for both controllers, they present similar settling time and overshoot. However, it was confirmed that one ROGI must be used for each phase-sequence that must be controlled. In addition, it can be seen (for both cases) that the use of a ROGI instead of a SOGI leads to a lower initial error. Then, considering the computational costs presented in Table 1 and the fact that their responses are very similar, ROGIs controllers are highly recommended for three-phase applications.

6.2 Application 2: Mitigation of the Harmonic Distortion Generated by a Three-Phase Rectifier

Figure 25 shows the block diagram of Application 2, while Table 2 displays the parameters of the prototype. The evaluated controllers were used in to control the variables i_{fa}, i_{fb} and i_{fc} of the SAPF. Thus, the transfer function of the plant in s-domain is

$$G_p(s) = \frac{\vec{i}_f(s)}{\vec{d}(s)} = \frac{\frac{V_{dc}}{R_f}}{1 + \frac{L_f}{R_f}s}, \tag{32}$$

in which the variable $\vec{d}(s)$ is the space vector obtained from the duty cycles in Laplace domain. The filter parameter L was chosen according to procedures commonly adopted in the literature (Wang et al. 2003). After the filter was constructed, the resulting resistance was measured.

Once again, in order to know which harmonic components the SAPF must control, it is necessary to evaluate the harmonic spectrum of the load currents (i_{la}, i_{lb} and i_{lc}). Figure 2 shows the harmonic spectrum of the current i_{la}. Thus, for the controller implementation in the phase quantities, it is necessary to control the family ($6k \pm 1$, $k \in \mathbb{N}$). Alternatively, Fig. 3 shows that for the controller implementation using vector notation, only

Table 3 Summary of the performance comparison between the controllers implemented in Application 2

Control scheme	K_i or K_{rc}	K_p	0dB gain crossing frequency (kHz)	Sensitivity index (Yepes et al. 2011)	VTHD of grid currents in steady-state operation (Neves et al. 2012) (%)	Settling time (5%) (ms)
(i) P + Multiple SOGIs (Yuan et al. 2002)	0.7	0.0473	1.9	0.32	3.02	24.3
(ii) P + Multiple ROGIs (Zeng et al. 2014)	1.4	0.0473	1.9	0.32	2.70	11.6
(iii) P + ($6k \pm 1$ RC) (Lu and Zhou 2011)	0.013	0.025	1.9	0.32	4.30	23.5
(iv) P + ($6k + 1$ RC) (Luo et al. 2016)	0.030	0.025	1.9	0.32	3.63	9.4
(v) $6k \pm 1$ RC (Neto et al. 2018c)	0.039	–	1.9	0.32	2.88	9.0
(vi) $6k + 1$ RC (Zimann et al. 2019)	0.060	–	1.9	0.32	2.65	6.4

The use of a real controller compromises more the system's stability than when using a complex controller. This fact stems from the high gain applied at high frequencies by the real RC, which could be avoided when using the complex RC. Therefore, complex RCs allow the use of greater controllers' gains.

In Application 2, six different control strategies were used:

(i) **P + Multiple SOGIs**: Implemented separately for α and β axes at the harmonics $h = \{1, 5, 7, 11, 13, 17, 19, 23, 25, 29\}$;
(ii) **P + Multiple ROGIs**: Implemented at the harmonics $h_s = \{+1, -5, +7, -11, +13, -17, +19, -23, +25, -$
(iii) **P + Real RC proposed in** (Lu and Zhou 2011): Implemented separately for α and β axes, with $n = 6$ and $m = 1$;
(iv) **P + Complex RC proposed in** (Luo et al. 2016): With parameters $n = 6$ and $m = 1$;
(v) **Real RC proposed in** (Neto et al. 2018c): Implemented separately for α and β axes, with $n = 6$ and $m = 1$;
(vi) **Complex RC proposed in** (Zimann et al. 2019): With parameters $n = 6$ and $m = 1$.

The stability evaluation and the controllers tuning of schemes (i) and (ii) were done using the sensitivity index (Yepes et al. 2011). As done in Application 1, all SOGIs and ROGIs were implemented with phase compensation, as suggested in (Yepes et al. 2011) and (Xie et al. 2017) for attenuating the effect of the computational delay. In (i), the same gain was used for all implemented SOGIs. In (ii), the same gain was used for all implemented ROGIs.

The methodology presented in (Neto et al. 2018b) was used to design all RC-based solutions. From this, the following parameters were obtained: The proportional and RC gains (K_p and K_{rc} in Table 3); a FIR filter (with order M), which is used to increase the system's relative stability; and a lead compensator, which is used to compensate the computational delay generated by digital implementation. In order to obtain a fair comparison, the same FIR filter and lead compensator were used for all RC-based schemes. The solutions (v) and (vi) are not implemented with proportional action because they have improved stability characteristics, making this action unnecessary.

Table 3 summarizes the experimental results for all evaluated controllers, indicating their vector total harmonic distortion (VTHD), which is used to characterize steady-state performance, and their settling time, which can be used as an indicator of the transient performance. Since strategies (ii), (iv) and (vi) can be obtained from the decomposition of the schemes (i), (iii) and (v), respectively, the performance comparison will be made between these pairs. Unlike Application 1, where the same gains were used for both evaluated controllers, for Application 2 the same stability

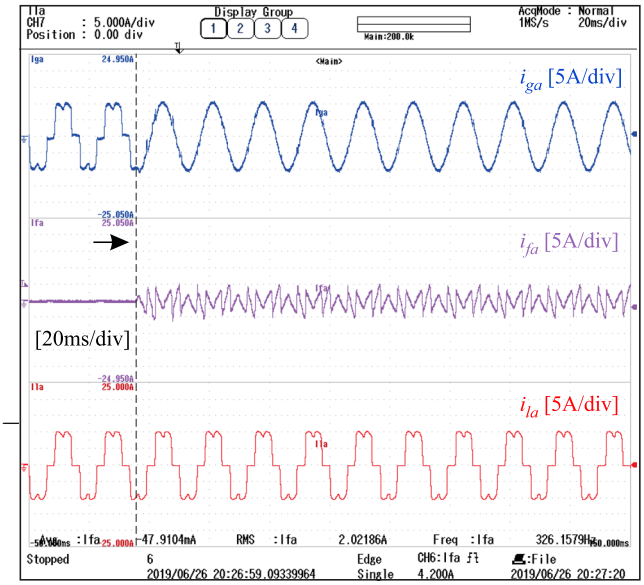

Fig. 26 Phase-a grid, APF output and load currents during control startup. Results obtained when using the complex RC proposed in Zimann et al. (2019)

characteristics and 0 db gain crossing frequency are wanted. Therefore, all complex control schemes will have greater resonant/repetitive gains than their equivalent real controllers, as discussed in Sect. 5.3. As consequence, it is observed that all complex controllers lead to better steady-state and better transient responses than the real controllers from which they are decomposed.

Figure 26 shows phase-a currents i_{ga}, i_{fa} and i_{la} during control startup when the complex RC proposed in (Zimann et al. 2019) is used. Since all control schemes are implemented in the $\alpha\beta$ reference frame, according to Table 1, they demand:

(i) 80 memory cells, 120 sums and 42 products;
(ii) 20 memory cells, 60 sums and 62 products;
(iii) 192 memory cells, 6 sums and 4 products;
(iv) 96 memory cells, 8 sums and 8 products;
(v) 192 memory cells, 6 sums and 6 products;
(vi) 96 memory cells, 6 sums and 8 products.

7 Conclusions

This paper presents a literature review of the main real and complex control schemes (based in the internal model principle) used for current control of three-phase inverters, whose reference signals can be represented a space vector. The viability of using this space vector as reference to three-phase control systems is mathematically evaluated. From this eval-

uation, it can be observed that complex controllers applied to space vectors require less memory cells than real controllers. In addition, these complex solutions present better steady-state performance, better transient performance and lower order than real controllers. Two experiments are used to confirm the theoretically predicted characteristics for practical applications, especially when it is desired to control multiple harmonic components.

Acknowledgements The authors would like to thank *Conselho Nacional de Desenvolvimento Científico e Tecnológico*—CNPq and *Fundação de Amparo à Ciência e Tecnologia do Estado de Pernambuco*—FACEPE, for the financial support.

References

Bhattacharya, S., et al. (1996). Parallel active filter system implementation and design issues for utility interface of adjustable speed drive systems. In *31th IEEE IAS* (Vol. 2, pp. 1032–1039).

Bojoi, R. I., et al. (2005). Current control strategy for power conditioners using sinusoidal signal integrators in synchronous reference frame. *IEEE Transactions on Power Electronics*, *20*(6), 1402–1412.

Bojrup, M., Karlsson, P., Alakula, M., & Gertmar, L. (1999). Multiple rotating integrator controller for active filters. In *Conf. Rec. EPE [CD-ROM]*.

Briz, F., Degner, M. W., & Lorenz, R. D. (2000). Analysis and design of current regulators using complex vectors. *IEEE Transactions on Industry Applications*, *36*(3), 817–825.

Busada, C. A., et al. (2012). Current controller based on reduced order generalized integrators for distributed generation systems. *IEEE Transactions on Industrial Electronics*, *59*(7), 2898–2909.

Buso, S., Malesani, L., & Mattavelli, P. (1998). Comparison of current control techniques for active filter applications. *IEEE Transactions on Industrial Electronics*, *45*(5), 722–729.

Escobar, G., Martinez, P. R., Leyva-Ramos, J., & Mattavelli, P. (2006). A negative feedback repetitive control scheme for harmonic compensation. *IEEE Transactions on Industrial Electronics*, *53*(4), 1383–1386.

Francis, B., & Wonham, W. (1975). The internal model principle for linear multivariable regulators. *Applied Mathematics and Optimization*, *2*(2), 170–194.

Ghetti, F. T., Barbosa, P. G., Braga, H. A. C., & Ferreira, A. A. (2010). Estudo comparativo de técnicas de controle de corrente aplicadas a filtros ativos shunt. In *XVIII Congresso Brasileiro de Automática* (pp. 3701–3708) (**in Portuguese**).

Hara, S., Omata, T., & Nakano, M. (1985). Synthesis of repetitive control systems and its application. In *24th IEEE CDC* (pp. 1387–1392). USA: Fort Lauderdale.

Hara, S., et al. (1988). Repetitive control system: a new type servo system for periodic exogenous signals. *IEEE Transactions on Automatic Control*, *33*(7), 659–668.

Inoue, T., Nakano, M., Kubo, T., Matsumoto, S., & Baba, H. (1981). High accuracy control of a proton synchrotron magnet power supply. *IFAC Proceedings Volumes*, *14*(2), 3137–3142.

Kazmierkowski, M. P., & Malesani, L. (1998). Current control techniques for three-phase voltage-source pwm converters: A survey. *IEEE Transactions on Industrial Electronics*, *45*(5), 691–703.

Lascu, C., Asiminoaei, L., Boldea, I., & Blaabjerg, F. (2007). High performance current controller for selective harmonic compensation in active power filters. *IEEE Transactions on Power Electronics*, *22*(5), 1826–1835.

Leonhard, W. (1996). *Control of electrical drives. Electrical engineering*. Berlin: Springer.

Limongi, L. R., et al. (2009). Digital current-control schemes. *IEEE Industrial Electronics Magazine*, *3*(1), 20–31.

Lu, W., & Zhou, K. (2011). A novel repetitive controller for nk ± m order harmonics compensation. In *30th Chinese control conference* (pp. 2480–2484).

Luo, Z., et al. (2016). A repetitive control scheme aimed at compensating the 6k + 1 harmonics for a three-phase hybrid active filter. *Energies*, *9*(10), 787.

Mattavelli, P., & Marafao, F. P. (2004). Repetitive-based control for selective harmonic compensation in active power filters. *IEEE Transactions on Industrial Electronics*, *51*(5), 1018–24.

Neto, R. C., de Souza, H. E. P., Neves, F. A. S., Azevedo, G. M. S., & Limongi, L. R. (2018a). Controladores complexos aplicados a vetores espaciais: Características e vantagens. In *XXII Congresso Brasileiro de Automática* (in Portuguese).

Neto, R. C., et al. (2018b). Design of repetitive controllers through sensitivity function. In *27th IEEE ISIE* (pp. 495–501).

Neto, R. C., et al. (2018c) A nk ± m-order harmonic repetitive control scheme with improved stability characteristics. In *27th IEEE ISIE* (pp. 465–470).

Neto, R. C., Neves, F. A. S., Azevedo, G. M. S., de Souza, H. E. P., & Batista, Y. N. (2018d). Structures of repetitive controllers based on GDSC with feedforward action. In *27th IEEE ISIE* (pp. 533–538).

Neves, F., et al. (2014). The SVFT-based control. *IEEE Transactions on Industrial Electronics*, *61*(8), 4152–4160.

Neves, F. A. S., de Souza, H. E. P., Cavalcanti, M. C., Bradaschia, F., & Bueno, E. J. (2012). Digital filters for fast harmonic sequence component separation of unbalanced and distorted three-phase signals. *IEEE Transactions on Industrial Electronics*, *59*(10), 3847–3859.

Neves, F. A. S., et al. (2009). A space-vector discrete Fourier transform for detecting harmonic sequence components of three-phase signals. In *35th IEEE IECON* (pp. 3631–3636).

Neves, F. A. S., et al. (2010). A space-vector discrete Fourier transform for unbalanced and distorted three-phase signals. *IEEE Transactions on Industrial Electronics*, *57*(8), 2858–2867.

Novotny, D., & Lipo, T. (1996). *Vector control and dynamics of AC drives No. v. 1 in Monographs in electrical and electronic engineering*. London: Clarendon Press.

Rodriguez, F. J., Bueno, E., Aredes, M., Rolim, L. G. B., Neves, F. A. S., & Cavalcanti, M. C. (2008). Discrete-time implementation of second order generalized integrators for grid converters. In *34th IEEE IECON* (pp. 176–181).

Rowan, T. M., & Kerkman, R. J. (1986). A new synchronous current regulator and an analysis of current-regulated pwm inverters. *IEEE Transactions on Industry Applications*, *22*(4), 678–690.

Shen, J., Schröder, S., Stagge, H., & Doncker, R. W. D. (2012). Precise modeling and analysis of DQ-frame current controller for high power converters with low pulse ratio. In *2012 IEEE energy conversion congress and exposition (ECCE)* (pp. 61–68).

Wang, T. C. Y., Zhihong, Y., Gautam, S., & Xiaoming, Y. (2003). Output filter design for a grid-interconnected three-phase inverter. In *34th IEEE PESC* (pp. 779–784).

Xie, C., et al. (2017). Reduced order generalized integrators with phase compensation for three-phase active power filter. In *2017 IEEE APEC* (pp. 2759–2766).

Yeh, S. C., & Tzou Y. Y. (1995) Adaptive repetitive control of a PWM inverter for ac voltage regulation with low harmonic distortion. In *26th IEEE PESC* (Vol. 1, pp. 157–163).

Yepes, A. G., et al. (2010). Effects of discretization methods on the performance of resonant controllers. *IEEE Transactions on Power Electronics*, *25*(7), 1692–1712.

Yepes, A. G., et al. (2011). Analysis and design of resonant current controllers for voltage-source converters by means of nyquist dia-

grams and sensitivity function. *IEEE Transactions on Industrial Electronics*, *58*(11), 5231–5250.

Yuan, X., et al. (2002). Stationary-frame generalized integrators for current control of active power filters with zero steady-state error for current harmonics of concern under unbalanced and distorted operating conditions. *IEEE Transactions on Industry Applications*, *38*(2), 523–532.

Zeng, Z., et al. (2014). Reduced order generalized integrators based selective harmonic compensation current controller for shunt active power filters. In *2014 IEEE ECCE* (pp. 1650–1655).

Zhou, K., Low, K. S., Wang, D., Luo, F. L., Zhang, B., & Wang, Y. (2006). Zero-phase odd-harmonic repetitive controller for a single-phase pwm inverter. *IEEE Transactions on Power Electronics*, *21*(1), 193–201.

Zimann, F. J., et al. (2019). A complex repetitive controller based on the generalized delayed signal cancelation method. *IEEE Transactions on Industrial Electronics*, *66*(4), 2857–2867.

Zmood, D. N., & Holmes, D. G. (1999). Stationary frame current regulation of PWM inverters with zero steady state error. In *30th IEEE PESC* (Vol. 2, pp 1185–1190).

Zmood, D. N., & Holmes, D. G. (2003). Stationary frame current regulation of PWM inverters with zero steady-state error. *IEEE Transactions on Power Electronics*, *18*(3), 814–822.

Publisher's Note Springer Nature remains neutral with regard to jurisdictional claims in published maps and institutional affiliations.

Fast Phase Angle Jump Estimation to Improve the Convergence Time of the GDSC-PLL

Daniel Soares dos Santos Andrade, Ygo Neto Batista, Francisco A. S. Neves, *Senior Member, IEEE*, and Helber Elias Paz de Souza

***Abstract*—The fast detection of magnitude, frequency, and phase angle of the fundamental-frequency component is very useful in many three-phase power system applications. Most techniques to accomplish this task are based on different versions of three-phase phase-locked loop (PLL) schemes. Some variables of three-phase systems may experience phase angle jumps after some disturbances. In this paper, a method for the fast detection of phase angle jump occurrence, estimation of the phase angle jump, and its use for improving the performance of the generalized delayed signal cancelation (GDSC) PLL is proposed. The proposed method is based on the detailed evaluation of the GDSC filter transient behavior after a phase jump. Results considering typical three-phase grid disturbances are used to evaluate the proposed scheme, in comparison with other usual PLL techniques. The use of the proposed phase jump angle estimator allowed a reduction in the GDSC-PLL convergence time of about 50%.**

***Index Terms*—Amplitude and phase estimation, power system harmonics, phase-locked loops (PLLs), synchronization method, phase jump.**

I. Introduction

THE phase-locked loop (PLL) is applied for phase, frequency, and amplitude estimation of selected harmonic components in a variety of crucial power system applications [1]–[3]. Among the various types of PLLs for three-phase systems, the synchronous reference frame PLL (SRF-PLL) is widely used [3]–[5].

In the SRF-PLL, the three-phase input voltages are transformed to the synchronous (dq) reference frame by applying the Clarke, and subsequently, the Park transformations. The dq reference frame angular position is then regulated using a feedback control loop, which forces v_q to zero in steady state [6]–[8], as shown in Fig. 1.

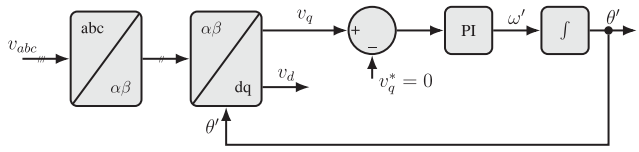

Fig. 1. Block diagram of the SRF-PLL.

The SRF-PLL is usually set to wide bandwidth in order to achieve fast phase estimation. However, for this case, the impact of low-order harmonics, unbalanced dc and fundamental-frequency negative-sequence (FFNS) components in the phase estimation are not acceptable for most applications. This issue is solved mostly by adding a prefilter to the SRF-PLL [3]. One of those prefilters is the generalized delayed signal cancellation (GDSC) [9], [10].

The GDSC applied as a prefilter for a classical three-phase PLL (GDSC-PLL) presents a good overall performance [9], [10]. This paper presents a scheme for greatly improving the GDSC-PLL convergence time in situations where phase jumps occur. We propose a scheme for very fast phase jump estimation and compensation, even in the polluted grid environment, in the presence of exponentially decaying dc component and under frequency variations.

II. Generalized Delayed Signal Cancellation (GDSC)

The GDSC is a digital filter in the stationary reference frame capable of eliminating any harmonic space vectors of positive or negative sequence. Its implementation is done by cascaded operations, each of which eliminates a family of harmonics, by using the signals previously sampled

$$\vec{f}_{\text{gdsc}}(kT_s) = \vec{a}\left\{\vec{s}_{\alpha\beta}(kT_s) + e^{j\theta_r}\,\vec{s}_{\alpha\beta}[(k-k_d)T_s]\right\} \quad (1)$$

in which T_s is the sampling period, kT_s is the current instant, $(k-k_d)T_s$ is the instant of delayed sample, and $\vec{a}$ is a complex gain.

The gain of the GDSC operation is given by

$$\vec{G}^{(h_s)} = \vec{a}[1 + e^{j(\theta_r - h_s \frac{2\pi}{N} k_d)}]. \quad (2)$$

Manuscript received October 3, 2018; revised December 29, 2018 and March 8, 2019; accepted March 30, 2019. Date of publication May 3, 2019; date of current version December 9, 2019. This work was supported by the Conselho Nacional de Desenvolvimento Cientfico e Tecnolgico—CNPq. *(Corresponding author: Francisco A. S. Neves.)*

D. S. S. Andrade and F. A. S. Neves are with the Power Electronics and Drives Research Group, Department of Electrical and Electronics Engineering, Universidade Federal de Pernambuco, 50740-530 Recife, Brazil (e-mail: danielsoares.andrade@gmail.com; fneves@ufpe.br).

Y. N. Batista and H. E. P. de Souza are with the Instituto Federal de Educação, Ciência e Tecnologia de Pernambuco, 55200-000 Pesqueira, Brazil (e-mail: ygo@pesqueira.ifpe.edu.br; helberelias@pesqueira.ifpe.edu.br).

Color versions of one or more of the figures in this paper are available online at http://ieeexplore.ieee.org.

Digital Object Identifier 10.1109/TIE.2019.2913823

0278-0046 © 2019 IEEE. Personal use is permitted, but republication/redistribution requires IEEE permission.
See http://www.ieee.org/publications_standards/publications/rights/index.html for more information.

Authorized licensed use limited to: Universidad Federal de Pernambuco. Downloaded on September 28,2020 at 17:29:55 UTC from IEEE Xplore. Restrictions apply.

TABLE I
PARAMETERS OF THE GDSC FOR FFPS COMPONENT ESTIMATION

Filter	θ_r (rad)	k_d	$\vec{a}$
A	π	$N/2$	$1/2$
B	$\pi/2$	$N/4$	$1/2$
C	$\pi/4$	$N/8$	$1/2$
D	$\pi/8$	$N/16$	$1/2$
E	$\pi/16$	$N/32$	$1/2$

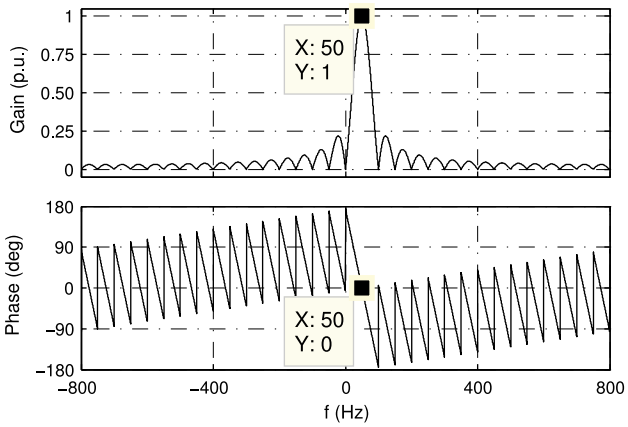

Fig. 2. Frequency response of the five GDSC cascaded operations.

In order to eliminate the harmonic component h_s, the gain must be null ($\vec{G}^{(h_s)} = 0$). Then, isolating the term h_s, we get [9]

$$h_s = \left(\frac{N\theta_r}{2\pi k_d} + \frac{N}{2k_d}\right) + \frac{N}{k_d}n \tag{3}$$

$$h_s = h_d + q + pn,\ n \in \mathbb{Z} \tag{4}$$

in which h_d is the desired harmonic component of the space vector, either positive or negative sequence, p is the periodicity of the eliminated harmonic components, and q is set to eliminate a specific harmonic.

The parameter θ_r required for the operation is given by

$$\theta_r = \frac{2\pi}{p}(h_d + q) - \pi. \tag{5}$$

The complex gain $\vec{a}$ is obtained so that the gain is unitary ($|\vec{G}^{(h_s)}| = 1$) for the desired harmonic component ($h_s = h_d$) as follows:

$$\vec{a} = \frac{1}{1 + e^{j\pi\left(\frac{2q}{p} - 1\right)}}. \tag{6}$$

Some operations must be cascaded to cancel different harmonic families. If we aim to get the fundamental-frequency positive-sequence (FFPS) component, the cascaded operations may be the A, B, C, D, and E, as designed in [9] and parameters shown in Table I. We named this filter output vector $\vec{f}_{\text{ABCDE}}(k)$. In fact, we use the term A-GDSC-PLL [9] since this approach is adaptive under frequency shift. The frequency response of the five cascaded operations is shown in Fig. 2.

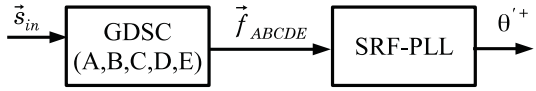

Fig. 3. Original GDSC-PLL scheme, according to [9].

III. OVERVIEW

Fig. 3 shows the original GDSC-PLL, according to [9] and Fig. 4 shows the proposed method. An overview of the blocks shown in Fig. 4 is presented in this section, while the implementation details are described in the next sections.

In order to start the phase jump compensation scheme, it is necessary first to detect the existence of a phase jump (*phase jump detector*). As soon as a phase jump is detected, the phase angle jump estimation is initialized (*init flag*). However, since certain severe disturbances could cause false indication of the phase jump, the use of the estimated phase angle jump remains disabled (*enable flag* $= 0$) for some time, without stopping the phase angle jump estimation process (*angle estimator*). The phase angle jump estimation is based on the evaluation of the GDSC filter transient behavior ($\vec{v}_R$). It should be observed that in the GDSC-PLL, as well as in usual PLL schemes, the output detected phase angle does not suffer abrupt changes but converges to the correct angle value after some time. For this reason, we cannot just sum the estimated phase angle jump (φ_e) to the GDSC-PLL output angle (*angle compensator*). The compensation angle ($\varphi_e - \Delta\theta$) starts with the estimated phase angle jump and gradually decreases to zero while the GDSC angle converges to the correct value. Furthermore, a modified SRF-PLL is proposed in order to enhance its performance right after the detection of the phase angle jump.

IV. PHASE JUMP COMPENSATION SCHEME

The proposed method is composed of three stages before SRF-PLL: detection, estimation, and compensation. The detection stage is based on the angular difference between the current and one cycle delayed GDSC output signals ($\vec{f}_{\text{ABCDE}}(k)$ and $\vec{f}_{\text{ABCDE}}(k-N)$), to generate phase jump flags. In the estimation stage, the current and one cycle delayed GDSC outputs are used for computing the phase angle jump. In the compensation stage, the estimated input phase jump is used to provide the correction of the $\vec{f}_{\text{ABCDE}}(k)$ angle during the GDSC transient.

A. Phase Jump Detector

The detection of the phase jump at the GDSC filter signal input is performed by monitoring the angular difference ($\Delta\theta$) between the current and one cycle delayed space vectors $\vec{f}_{\text{ABCDE}}(k)$ and $\vec{f}_{\text{ABCDE}}(k-N)$

$$\Delta\theta(k) = \angle\left[\frac{\vec{f}_{\text{ABCDE}}(k)}{\vec{f}_{\text{ABCDE}}(k-N)}\right]. \tag{7}$$

If the angle between these vectors starts increasing (or decreasing), it may mean a phase jump. Thus, the rate of change of that parameter is analyzed. To follow the dynamics, we calculate the

Authorized licensed use limited to: Universidad Federal de Pernambuco. Downloaded on September 28,2020 at 17:29:55 UTC from IEEE Xplore. Restrictions apply.

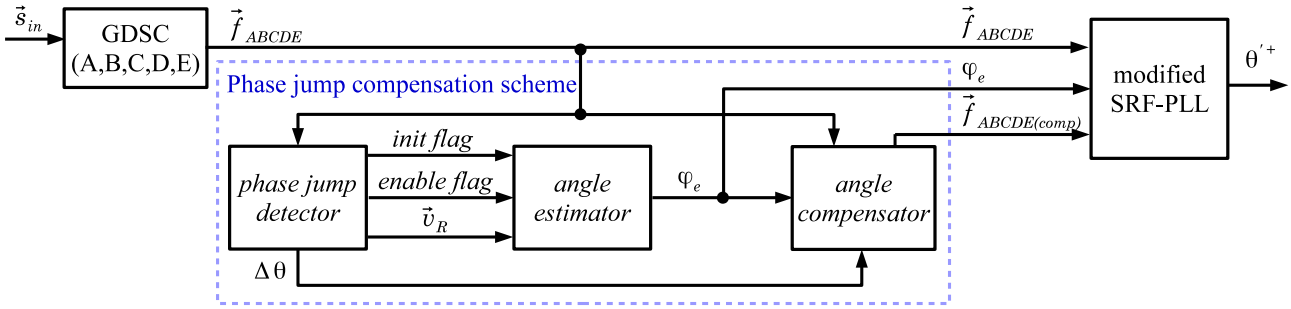

Fig. 4. Overview of the method applied to GDSC.

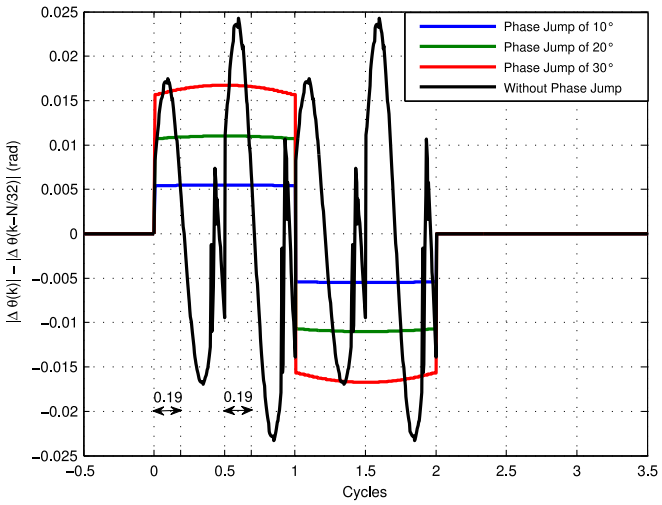

Fig. 5. Tests for selecting the phase jump detection threshold ε. $|\Delta\theta(k)| - |\Delta\theta(k - N/32)|$ for an FFPS signal that experiences only phase jumps (without harmonic components) or without phase jump (the disturbance corresponds to a phase-to-phase fault, with positive- and negative-sequence fundamental-frequency components having the same amplitude).

difference between $|\Delta\theta(k)|$ and $|\Delta\theta(k - N/32)|$, since $N/32$ is the delay of the fastest operation, among the five cascade operations that compose the GDSC filter. If this difference is greater than a limit value (threshold value) ε as

$$|\Delta\theta(k)| - |\Delta\theta(k - N/32)| > \varepsilon \tag{8}$$

the flag of initialization (*init flag*) is triggered to logic level 1. ε must be big enough to avoid the false indication of the phase jump due to other types of disturbances. On the other hand, ε must be small enough for ensuring good sensitivity to phase jump occurrence. To choose the value of ε, we plotted, in Fig. 5, $|\Delta\theta(k)| - |\Delta\theta(k - N/32)|$ after different phase angle jumps and severe grid disturbances. It was observed that the detector identifies phase jumps from 10º when the adjusted value of ε is 5×10^{-3}. However, it can be observed that the value of $|\Delta\theta(k)| - |\Delta\theta(k - N/32)|$, during a disturbance without the phase jump, experiences oscillations around zero whose amplitude may exceed the threshold $\varepsilon = 5 \times 10^{-3}$. The frequency of these oscillations is $|1 - h_s|\omega_1$. Several simulations of disturbances without considering phase jumps were then performed and the time intervals during which the phase jump detector remained activated were observed. The worst practical situation was the occurrence of positive- and negative-sequence components with the same amplitude, situation that occurs during single- or two-phase faults. In this extreme case, the phase jump detector remained activated for 0.19 fundamental period, approximately, as shown in Fig. 5.

The value of the threshold ε as well as the time for generation of the enabling pulse can be adjusted according to the application and severity of the disturbances expected in the power system.

In our implementation, the jump detection signal (*init flag*) is the input to a timer and, if it stays active for more than 30% of one fundamental period, the signal *enable flag* switches to 1, indicating the phase jump confirmation. Thus, the system initializes the estimation process with *init flag* and enables the result with *enable flag*. This timing prevents disturbances such as severe unbalances from being confused with the phase jump. The block diagram of this detector can be seen in the area marked in Fig. 6.

B. Angle Estimator

The angle estimation is performed in four stages. Initially, we developed a mathematical model for the GDSC response when it is processing a signal with phase jump. Then, based on this model, we developed an algorithm for estimating the phase angle. However, other disturbances may be present in the electrical network. Therefore, an improvement in the technique is then proposed for avoiding the influence of severe distortions on the angle estimation. Finally, we inserted a filter to smooth the convergence.

1) Development of the GDSC Mathematical Model: We develop a compact equivalent model for GDSC filters of Table I, using the general form of the GDSC operation (1). Connecting the operation A output to the operation B input, we obtain

$$\vec{f}_{AB}(k) = (1/2)^2[\vec{s}_{\alpha\beta}(k) + e^{j\pi/2}\vec{s}_{\alpha\beta}(k - N/4) + e^{j\pi}\vec{s}_{\alpha\beta}(k - N/2) + e^{j3\pi/2}\vec{s}_{\alpha\beta}(k - 3N/4)]. \tag{9}$$

Connecting the other GDSC operations (C, D, and E) and after some mathematical manipulations, the response of the filter is

Authorized licensed use limited to: Universidad Federal de Pernambuco. Downloaded on September 28,2020 at 17:29:55 UTC from IEEE Xplore. Restrictions apply.

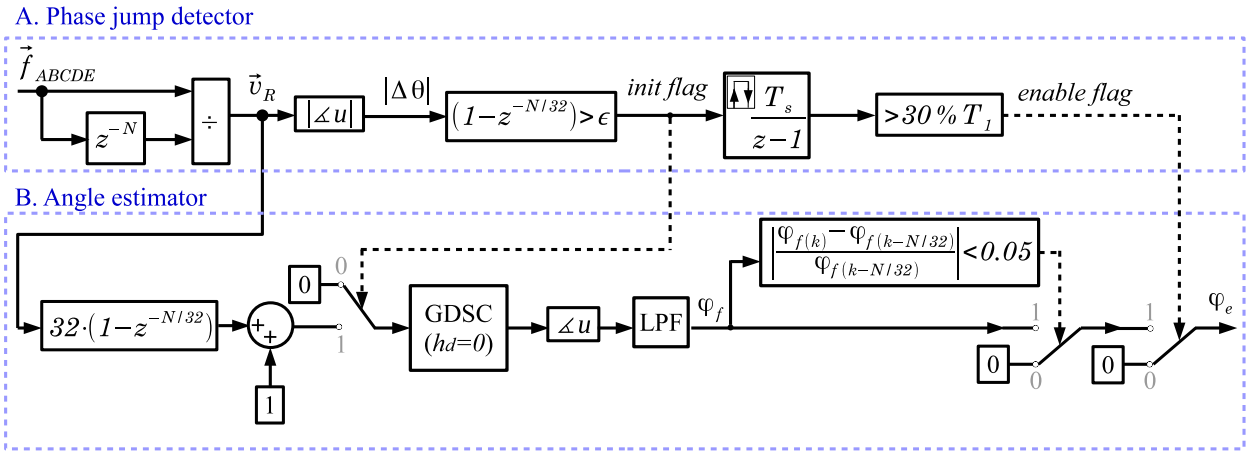

Fig. 6. Diagram of detection and estimation procedures.

obtained as

$$\vec{f}_{\mathrm{ABCDE}}(k)=\frac{1}{32}\sum_{n=0}^{31}e^{\left(\frac{j\pi n}{16}\right)}\vec{s}_{\alpha\beta}\left(k-n\frac{N}{32}\right). \tag{10}$$

Then, in order to obtain the response of the GDSC filter after a phase jump, we model the input signal as

$$\vec{s}_{\alpha\beta}(k)=\vec{v}_{1(\mathrm{pre})}(k)\left[1-H(k)\right]+\vec{v}_{1(\mathrm{post})}(k)H(k) \tag{11}$$

where $H(k)$ is the unit step function, $\vec{v}_{1(\mathrm{pre})}(k)$ is the steady-state FFPS space vector sampled before the phase jump, and $\vec{v}_{1(\mathrm{post})}(k)$ is the steady-state FFPS space vector after the phase jump: $\angle\vec{v}_{1(\mathrm{post})}(k)=\angle[\vec{v}_{1(\mathrm{pre})}(k)]+\varphi$. The presence of harmonics and nonperiodic components in the input signals is considered later.

The signals $\vec{v}_{1(\mathrm{pre})}(k)$ and $\vec{v}_{1(\mathrm{post})}(k)$ can be written as

$$\vec{v}_{1(\mathrm{pre})}(k)=V_{1(\mathrm{pre})}e^{j\theta_0}e^{j\omega_1 kT_s} \tag{12}$$

and

$$\vec{v}_{1(\mathrm{post})}(k)=V_{1(\mathrm{post})}e^{j(\theta_0+\varphi)}e^{j\omega_1 kT_s}. \tag{13}$$

Substituting (12) and (13) into (11) and the result in (10) gives

$$\begin{aligned}\vec{f}_{\mathrm{ABCDE}}(k)=&\frac{1}{32}\\&\times\sum_{n=0}^{31}e^{\frac{j2\pi}{32}n}\left\{\vec{v}_{1(\mathrm{pre})}\left(k-n\frac{N}{32}\right)\left[1-H\left(k-n\frac{N}{32}\right)\right]\right.\\&\left.+\vec{v}_{1(\mathrm{post})}\left(k-n\frac{N}{32}\right)H\left(k-n\frac{N}{32}\right)\right\}.\end{aligned} \tag{14}$$

Observing that, from (12) and (13)

$$\vec{v}_{1(\mathrm{pre})}\left(k-n\frac{N}{32}\right)=e^{\left(-\frac{j2\pi}{32}n\right)}\vec{v}_{1(\mathrm{pre})}(k)$$

$$\vec{v}_{1(\mathrm{post})}\left(k-n\frac{N}{32}\right)=e^{\left(-\frac{j2\pi}{32}n\right)}\vec{v}_{1(\mathrm{post})}(k)$$

and that

$$H\left(k-n\frac{N}{32}\right)=\begin{cases}0,\ \text{if } k<n\frac{N}{32}\ \left(\text{i.e., } n>\frac{32k}{N}\right)\\1,\ \text{if } k\geqslant n\frac{N}{32}\ \left(\text{i.e., } n\leqslant\frac{32k}{N}\right)\end{cases}$$

then

$$\vec{f}_{\mathrm{ABCDE}}(k)=\left[1-\gamma(k)\right]\vec{v}_{1(\mathrm{pre})}(k)+\gamma(k)\vec{v}_{1(\mathrm{post})}(k) \tag{15}$$

in which

$$\gamma(k)=\frac{1}{32}\left[1+\mathrm{floor}\left(\frac{k}{N/32}\right)\right]. \tag{16}$$

The expression (15) shows that the phase jump at the operation A input, does not have an immediate effect on the operation E output. The obtained response shows that, each $N/32$ samples, the space vector $\vec{v}_{1(\mathrm{pre})}(k)/32$ is subtracted from the filter output while, simultaneously, $\vec{v}_{1(\mathrm{post})}(k)/32$ is added to the filter output signal. This behavior continues until $\gamma(k)=1$, when $\vec{v}_{1(\mathrm{pre})}(k)$ is fully canceled and $\vec{v}_{1(\mathrm{post})}(k)$ is completely found on the output.

2) Phase Angle Jump Estimation: During the GDSC transient due to phase jump we assume at first that the frequency has not been significantly changed and define the space vector $\vec{v}_R$ as

$$\vec{v}_R(k)=\frac{\vec{f}_{\mathrm{ABCDE}}(k)}{\vec{f}_{\mathrm{ABCDE}}(k-N)}=\frac{\vec{f}_{\mathrm{ABCDE}}(k)}{\vec{v}_{1(\mathrm{pre})}(k)}. \tag{17}$$

It is worth noting that the filter output signal is in steady state before the phase jump. In other words, $\vec{f}_{\mathrm{ABCDE}}(k-N)=\vec{v}_{1(\mathrm{pre})}(k)$ is taken as a reference during the GDSC transient. Knowing the GDSC filter output after a phase jump (15) and after a few mathematical manipulations, $\vec{v}_R$ is written as

$$\vec{v}_R(k)=1-\gamma(k)+\gamma(k)(V_{1(\mathrm{post})}/V_{1(\mathrm{pre})})e^{j\varphi}. \tag{18}$$

It can be observed from (16) that

$$\Delta\gamma=\begin{cases}\frac{1}{32}, & \text{if } k+1=m\frac{N}{32},\ m\in\mathbb{Z}\\0, & \text{otherwise.}\end{cases}$$

Authorized licensed use limited to: Universidad Federal de Pernambuco. Downloaded on September 28,2020 at 17:29:55 UTC from IEEE Xplore. Restrictions apply.

In other words, every $N/32$ samples, $\gamma(k)$ varies $1/32$. Therefore, every $N/32$ samples $\vec{v}_R(k)$ changes according to

$$\Delta\vec{v}_R = -\Delta\gamma + \Delta\gamma\frac{V_{1(\text{post})}}{V_{1(\text{pre})}}e^{j\varphi} = \frac{1}{32}\left[-1 + \frac{V_{1(\text{post})}}{V_{1(\text{pre})}}e^{j\varphi}\right]. \quad (19)$$

Then

$$32\Delta\vec{v}_R + 1 = \frac{V_{1(\text{post})}}{V_{1(\text{pre})}}e^{j\varphi} \quad (20)$$

and

$$\angle\left(32\Delta\vec{v}_R + 1\right) = \varphi. \quad (21)$$

From (21), we realized that it is possible to obtain the phase angle jump immediately for the case when only phase jump occurs

$$\varphi = \angle\left\{32[\vec{v}_R(k) - \vec{v}_R(k - N/32)] + 1\right\} \quad (22)$$

where $\vec{v}_R$ is obtained from (17), using the current and one cycle delayed GDSC filter outputs.

Let us consider now that the disturbance causes not only a phase angle jump in the FFPS component, but also introduces harmonic and nonperiodic signals. In this case, the disturbance leads the GDSC filter output to

$$\vec{f}_{\text{ABCDE}}(k) = [1 - \gamma(k)]\,\vec{v}_{1(\text{pre})}(k) + \gamma(k)\vec{v}_{1(\text{post})}(k) + \vec{f}_h(k) + \vec{f}_{\text{non}-p}(k) \quad (23)$$

in which $\vec{f}_h(k)$ is the term related to harmonic components of positive and negative sequences, while $\vec{f}_{\text{non}-p}(k)$ is related to nonperiodic components, such as exponential and dc components. Once both $\vec{f}_h(k)$ and $\vec{f}_{\text{non}-p}(k)$ influence the phase jump estimation, a filter was used to attenuate their effect. Due to space restrictions, this filter is analyzed considering only $\vec{f}_{\text{non}-p}(k)$, which includes the exponentially decaying dc component usually present in grid disturbances. However, it can be demonstrated that the filter provides attenuation also to $\vec{f}_h(k)$. Repeating the procedure that led us to (21), we obtain

$$\vec{v}_R(k) = 1 - \gamma(k) + \gamma(k)\frac{V_{1(\text{post})}}{V_{1(\text{pre})}}e^{j\varphi} + \frac{\vec{f}_{\text{non}-p}(k)}{\vec{v}_{1(\text{pre})}(k)}. \quad (24)$$

Consequently

$$\Delta\vec{v}_R = -\Delta\gamma + \Delta\gamma\frac{V_{1(\text{post})}}{V_{1(\text{pre})}}e^{j\varphi} + \Delta\left(\frac{\vec{f}_{\text{non}-p}}{\vec{v}_{1(\text{pre})}}\right). \quad (25)$$

Remembering that each $N/32$ samples, $\gamma(k)$ varies $1/32$, follows:

$$32\Delta\vec{v}_R + 1 = \frac{V_{1(\text{post})}}{V_{1(\text{pre})}}e^{j\varphi} + 32\Delta\left(\frac{\vec{f}_{\text{non}-p}}{\vec{v}_{1(\text{pre})}}\right) \quad (26)$$

TABLE II
PARAMETERS OF THE GDSC FOR DC COMPONENT ESTIMATION

Filter	θ_r (rad)	k_d	$\vec{a}$
A	0	$N/2$	$1/2$
B	0	$N/4$	$1/2$
C	0	$N/8$	$1/2$
D	0	$N/16$	$1/2$
E	0	$N/32$	$1/2$

or

$$32[\vec{v}_R(k) - \vec{v}_R(k - N/32)] + 1 = \frac{V_{1(\text{post})}}{V_{1(\text{pre})}}e^{j\varphi} + 32\Delta\left(\frac{\vec{f}_{\text{non}-p}}{\vec{v}_{1(\text{pre})}}\right). \quad (27)$$

The nonperiodic component causes an error in the estimated phase angle jump φ computed though the phase angle of the left-hand-side term of (27). Note that the term containing the phase angle jump φ is constant, while the term related to the nonperiodic component varies in time. Then, the constant term can be isolated by a GDSC filter ($h_d = 0$). This low-pass filter was designed as described in [9] and [10] and its parameters are summarized in Table II. It has been shown [11] that the GDSC filter with a clean buffer has the property of instantaneously presenting in the output a signal with the same phase angle of the input, although attenuated (in this case by $1/32$). For this reason, the input of the GDSC filter applied to the signal (27) remains equal to zero until the *init flag* level becomes one.

3) Estimated Angle Filtering: After estimating the phase angle jump almost instantaneously, it is advisable to filter this value since severe disturbances in the electrical grid may generate hasty oscillations in the estimated angle. Once the estimated value is constant in cases of pure phase jumps, we inserted a second-order Butterworth LPF, with cut-off frequency of 300 Hz, followed by a switch that enables the LPF output (φ_f) whenever the φ_f oscillation is below an user-defined threshold, as in (28), as it can be seen in Fig. 6.

$$\left|\frac{\varphi_f(k) - \varphi_f(k - N/32)}{\varphi_f(k - N/32)}\right| < 0.05. \quad (28)$$

In order to keep the angle estimation at zero whenever a phase jump is not detected, we only enable the output if the phase jump is confirmed. In that case, the estimated and filtered phase angle (φ_f) is used to accelerate the convergence of the SRF-PLL. In Fig. 6, we see the diagram that summarizes the detection and estimation steps.

C. Angle Compensator

Under steady-state operation and before the occurrence of a phase jump, the angular position of $\vec{f}_{\text{ABCDE}}(k)$ is given by $(\omega_1 kT_s + \theta_0)$. When the input signal $\vec{s}_{\text{in}}$ (see Fig. 3) experiences a phase jump φ, since the GDSC buffer had been filled out, the phase angle of the $\vec{f}_{\text{ABCDE}}(k)$ does not converge to the correct value $(\omega_1 kT_s + \theta_0 + \varphi)$ instantaneously, as shown in Fig. 7.

Authorized licensed use limited to: Universidad Federal de Pernambuco. Downloaded on September 28,2020 at 17:29:55 UTC from IEEE Xplore. Restrictions apply.

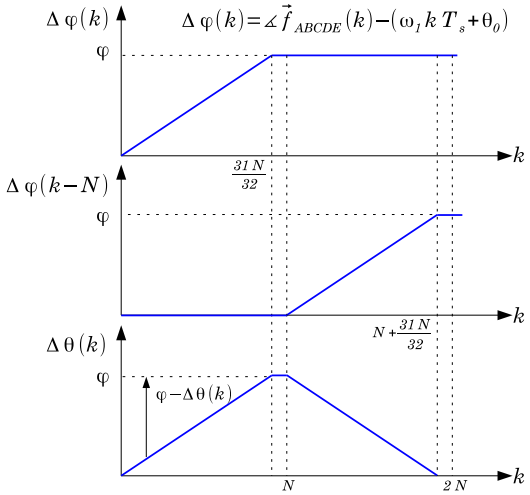

Fig. 7. Space vector angle correction during a transient after a phase jump.

The phase angle of $\vec{f}_{\text{ABCDE}}(k-N)$ starts to be influenced by the phase jump in the Nth sample, converging to the value $(\omega_1 kT_s + \theta_0 + \varphi)$ in the sample $(N + 31N/32)$. The difference between these angular positions is also presented in Fig. 7. In order to fix the phase angle of $\vec{f}_{\text{ABCDE}}(k)$ using the estimated phase angle jump, during the transient in which the phase angle of $\vec{f}_{\text{ABCDE}}(k)$ is converging to the correct value, we can then sum $\varphi - \Delta\theta(k)$ to it. This sum must occur as long as the rate of change of $|\Delta\theta(k)|$ is positive. In fact, when the rate of change of $|\Delta\theta(k)|$ is negative, the signal *init flag* becomes zero (see Fig. 6).

V. Modified SRF-PLL

In the original version of the GDSC-based synchronization method, the GDSC outputs the FFPS component of a three-phase grid ($\vec{f}_{\text{ABCDE}}$), which is used by the SRF-PLL to estimate its phase angle and amplitude. Right after a phase jump, the GDSC filter takes almost one cycle to converge. In this case, the original SRF-PLL with a proportional–integral (PI) controller, as in [9], [12], and [13], can keep pace with the convergence of the GDSC.

However, the purpose of the new system described up until now is to fast and accurately update the angle of $\vec{f}_{\text{ABCDE}}$, now named $\vec{f}_{\text{ABCDE(comp)}}$, according to the angle of the grid. Unlike $\vec{f}_{\text{ABCDE}}$, $\vec{f}_{\text{ABCDE(comp)}}$ can experience phase angle steps. Then, one of this paper contributions consists in modifying the SRF-PLL control structure after a phase jump in order to improve its overall performance.

If the SRF-PLL continued using only the PI controller, it would have an overshoot in the estimated phase angle right after a phase jump. So, we propose to adapt the controller according to the phase angle jump estimation in order to decrease the convergence time. If a phase jump is detected, an SRF-PLL with only proportional (P) controller is applied. Else, the PI controller is used. When switching from P to PI controller, the integrator has its buffer cleared, since integrating the error after a phase jump would also cause overshoot.

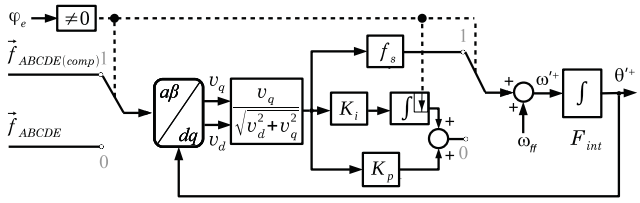

Fig. 8. High-performance SRF-PLL for the GDSC.

The choice of the gain for the P controller is based on the deadbeat method [14]–[16]. Considering that the transfer function of the SRF-PLL integrator that delivers the estimated angle is

$$F_{\text{int}}(z) = \frac{T_s}{z-1} \tag{29}$$

and considering the design of a deadbeat controller, we get the controller transfer function

$$P(z) = \frac{1}{F_{\text{int}}(z)(z-1)} = f_s \tag{30}$$

in which f_s is the sampling frequency. In fact, the deadbeat action can be understood as follows.

If at some sampling instant, the angular position of the FFPS vector $\vec{v}^+$ in the $\alpha\beta$ plane is θ^+, but the SRF-PLL output angle θ'^+ is different from this value, then the calculated q-axis voltage component is equal to $v_q'^+ = |\vec{v}^+|\sin(\theta^+ - \theta'^+)$. Considering that the angle error is small, then $\sin(\theta^+ - \theta'^+) \approx (\theta^+ - \theta'^+)$. Thus, if the PI controller is temporarily replaced by $f_s = 1/T_s$, then

$$\theta'^+ = \frac{1}{T_s}F_{\text{int}}(z)\frac{v_q'^+}{|\vec{v}^+|} \approx \frac{1}{T_s}\frac{T_s}{z-1}(\theta^+ - \theta'^+). \tag{31}$$

Therefore, $\theta'^+_{k+1} \approx \theta^+_k$ and a deadbeat control behavior is achieved. To take into consideration the nominal angular speed of vector $\vec{v}^+$, the feedforward action ω_{ff} can be added to the integrator input.

In this way, the controller is no longer fixed but a switched function according the phase jump detection, as depicted in Fig. 8.

VI. Simulation Results

To verify the effectiveness of the proposed method, we performed simulations of three case studies using DDSRF-PLL, DSOGI-PLL, A-GDSC-PLL, and A-GDSC-PLL with phase jump compensation. The compensation schemes were compared considering step, ramp, and exponential changes in the supply conditions, together with unbalance and harmonic distortions. For obtaining these results, the parameters of each implemented method were maintained.

In order to ensure a fair comparison, the DDSRF-PLL and DSOGI-PLL had their parameters calculated according to the methodology found in [4] and [17], while the A-GDSC-PLL design followed the methodology in [9]. The sampling frequency was set at 12.8 kHz and the nominal grid phase voltage amplitude and frequency were 100 V and 50 Hz. In all simulation results, the voltages were indicated in percent of the rated value.

Authorized licensed use limited to: Universidad Federal de Pernambuco. Downloaded on September 28,2020 at 17:29:55 UTC from IEEE Xplore. Restrictions apply.

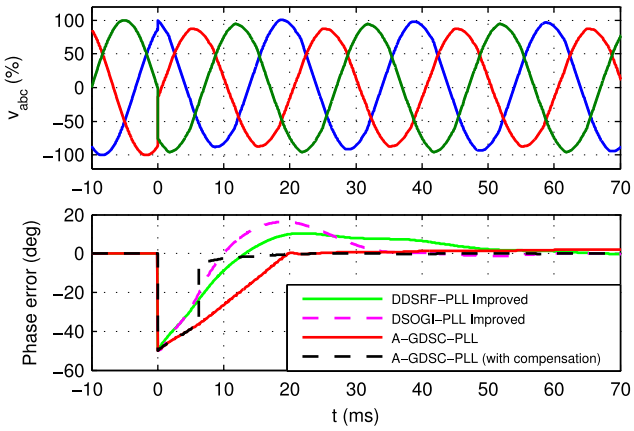

Fig. 9. Input voltages and phase errors for PLLs in Case 1.

Before the disturbances, the system was running at the nominal balanced sinusoidal condition.

The case tests were based on the standard IEC 61000. We have tried to consider significant amount of positive- and negative-sequence components, since this is a frequent situation during unbalanced faults. Further, even harmonics also appear due to saturation of transformers. Finally, there typically appear odd harmonic components and exponentially decaying dc components. The objective of including a wide range of harmonic components is to show that the usefulness of our proposal is not limited to situations where only a limited set of odd harmonics are expected to occur. Examples of application are power systems protection and control of distributed generation units connected to high-voltage grids.

Additionally, the proposed A-GDSC-PLL with phase jump compensation was compared with other recent synchronization schemes. Some test cases presented in [18]–[20] were reproduced using the proposed method and the results were compared with those obtained by the respective authors.

A. Case 1: Phase Jump Simultaneous With Light Disturbances

The simulation consists of simultaneous $+50°$ phase jump and other disturbances. Slight voltage sag and FFNS components: $V_1^+ = 92\%$ and $V_1^- = 5\%$; typical nontriple odd harmonic components: $V_5^- = 0.6\%$, $V_7^+ = 0.6\%$, $V_{11}^- = 0.3\%$, $V_{13}^+ = 0.3\%$, $V_{17}^- = 0.2\%$, and $V_{19}^+ = 0.2\%$; triple harmonics: $V_3^+ = 0.2\%$, $V_6^+ = 0.1\%$, $V_9^+ = 0.1\%$, and $V_{15}^+ = 0.1\%$, and some even harmonic components: $V_2^+ = 0.3\%$, $V_4^+ = 0.2\%$, and $V_8^+ = 0.1\%$. Besides, an exponentially decaying dc component with a time constant of 30 ms is added to the Phase A and its initial amplitude is 10% of the nominal peak value.

The results of the simulation are summarized in Fig. 9 and Table III. We noticed that while the A-GDSC-PLL with compensator presents the shortest settling time (0.85 cycle), the DDSRF-PLL has the longest settling time (about three cycles), and DSOGI-PLL has the highest phase angle error overshoot $(16.32°)$.

TABLE III
TABLE OF RESULTS FOR CASE 1

	The 2% settling time	phase error overshoot
A-GDSC-PLL (with compensation)	0.85 cycle	-
A-GDSC-PLL	1 cycle	-
DSOGI-PLL	1.7 cycle	16.32°
DDSRF-PLL	3.1 cycle	10.44°

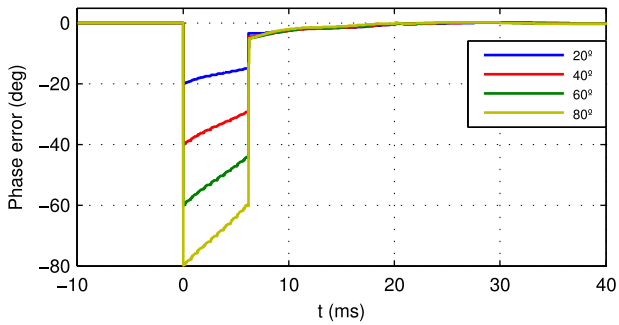

Fig. 10. Phase angle errors for the A-GDSC-PLL with phase jump compensation in Case 1.

TABLE IV
TABLE OF RESULTS FOR CASE 2

	The 2% settling time	phase error overshoot
A-GDSC-PLL (with compensation)	0.5 cycle	-
A-GDSC-PLL	1 cycle	-
DSOGI-PLL	2.4 cycle	−7.76°
DDSRF-PLL	2.8 cycle	−18.5°

Still for this test case, we simulated the occurrence of phase jumps sweeping from 20° to 80° with steps of 20°. The results for the A-GDSC-PLL with the compensator are in Fig. 10, in which we observe that the performance of the phase jump estimation was similar regardless the jump angle. The 2% settling times are practically the same and the method required only the minimum time for the phase jump confirmation.

B. Case 2: Simultaneous Phase Jump, Harmonics, and Frequency Variation

This case consists of phase jump of $-40°$, with $V_1^+ = 100\%$ simultaneous with other disturbances: FFNS component $V_1^- = 10\%$, and the most prominent odd harmonics $V_7^+ = 5\%$, and $V_5^- = 10\%$. The frequency varies in ramp from 50 to 50.1 Hz with a slope of 0.1 Hz/s.

The results of the simulation are summarized in Fig. 11 and Table IV. We found that while the A-GDSC-PLL with compensation has the lowest settling time (0.5 cycle) and the DDSRF-PLL had the longest settling time (2.8 cycles), the DSOGI-PLL had the highest phase angle error overshoot $(-18.5°)$.

For this same case, we evaluated the effectiveness of the method for the occurrence of phase jumps of $-20°$ to $-80°$ with

Authorized licensed use limited to: Universidad Federal de Pernambuco. Downloaded on September 28,2020 at 17:29:55 UTC from IEEE Xplore. Restrictions apply.

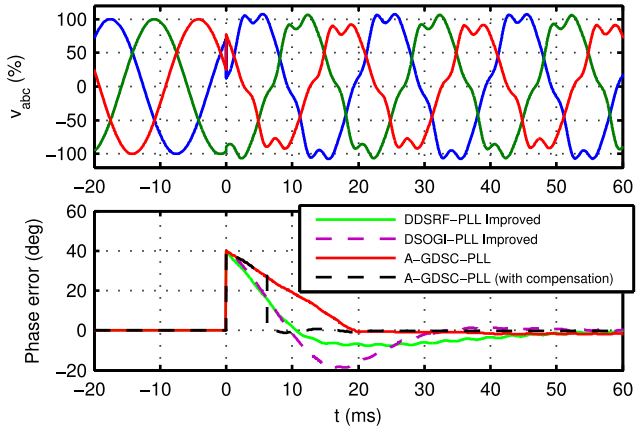

Fig. 11. Input voltages and phase errors for PLLs in Case 2.

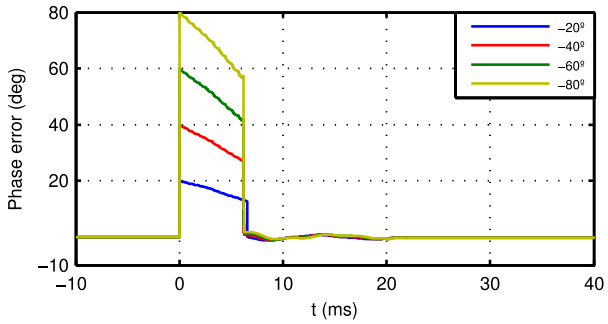

Fig. 12. Phase angle errors for the A-GDSC-PLL with phase jump compensation in Case 2.

steps of -20° in Fig. 12. We observed that the performance was similar regardless the jump angle.

C. Case 3: Large Phase Jump Simultaneously With Severe Disturbances

We simulated the simultaneous phase jump of -60° with other severe disturbances. Voltage sag and strong unbalance: $V_1^+ = 50\%$ and $V_1^- = 30\%$; nontriple odd harmonic components: $V_5^- = 2.5\%$, $V_7^+ = 2.5\%$, $V_{11}^- = 2.0\%$, $V_{13}^+ = 2\%$, $V_{17}^- = 1.0\%$, $V_{19}^+ = 1\%$, $V_{23}^- = 0.2\%$, and $V_{25}^+ = 0.2\%$; triple harmonic components: $V_3^+ = 0.7\%$, $V_6^+ = 0.2\%$, $V_9^+ = 0.7\%$, $V_{12}^+ = 0.1\%$, $V_{15}^+ = 2\%$, $V_{18}^+ = 0.1\%$, $V_{21}^+ = 0.1\%$, and $V_{24}^+ = 0.1\%$; and even harmonic components: $V_2^+ = 1\%$, $V_4^+ = 0.5\%$, $V_8^+ = 0.1\%$, $V_{10}^+ = 0.1\%$, $V_{14}^+ = 0.1\%$, $V_{16}^+ = 0.1\%$, $V_{20}^+ = 0.1\%$, and $V_{22}^+ = 0.1\%$.

Besides, an exponentially decaying dc component with a time constant of 30 ms is added to the signal of phase A. The initial amplitude of the dc component is equal to the nominal peak value of the FFPS. In this case, the frequency varies in ramp from 50 to 48 Hz with slope of -1 Hz/s.

The results of the simulation are summarized in Fig. 13 and Table V. We noticed that the A-GDSC-PLL with a phase jump compensation scheme decreases the phase error during the transient of the GDSC. We removed the DSOGI-PLL because it became unstable.

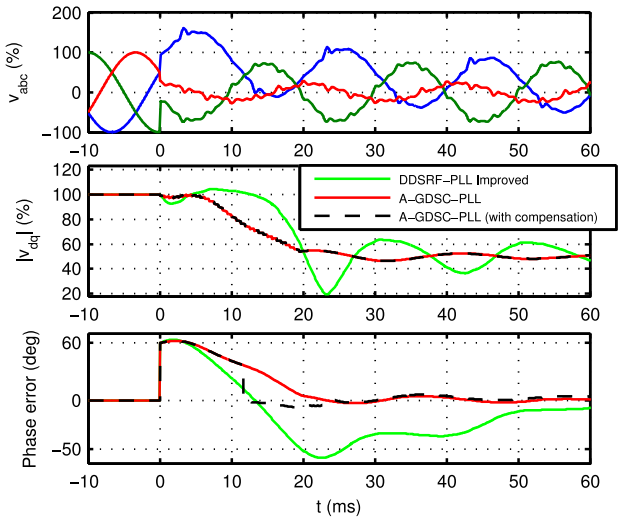

Fig. 13. Input voltages and phase errors for PLL in Case 3.

TABLE V
TABLE OF RESULTS FOR CASE 3

	The 2% settling time	phase error overshoot
A-GDSC-PLL (with compensation)	5.5 cycles	-6.9°
A-GDSC-PLL	8.1 cycles	-2.3°
DDSRF-PLL	5.7 cycles	-59.2°

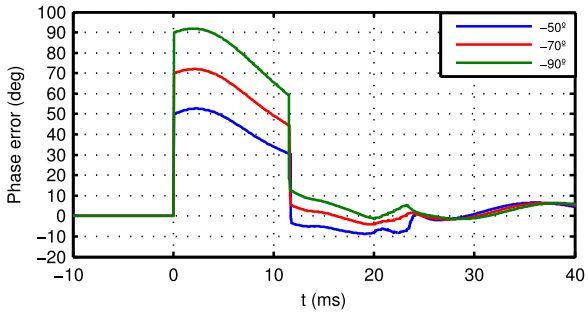

Fig. 14. Phase errors for jump phase of $-$ 50º, $-$ 70º, and $-$ 90º in Case 3.

We also performed the test case considering several different phase jumps with these perturbations as shown in Fig. 14. We notice that the A-GDSC-PLL with phase jump compensation shows improvements in the transient characteristics even for large phase jumps.

D. Comparison With Other Recent Synchronization Schemes

For additional evaluation of the proposed method, some test cases presented in papers about recent synchronization schemes were simulated using our proposal. The results obtained are then compared with those shown in the original papers.

In [18], the authors investigate MDSC-based 3P-EPLL intending to improve synchronization methods. We have simulated two test cases presented by the authors.

Authorized licensed use limited to: Universidad Federal de Pernambuco. Downloaded on September 28,2020 at 17:29:55 UTC from IEEE Xplore. Restrictions apply.

1) Distorted grid voltage: Even harmonics $h = +2, -4, +8$, and -10 with amplitude $V_h = 1/(4h)/2$, odd harmonics $h = -5, +7, -11, +13, -17$, and $+19$ with amplitude $V_h = 1/(4h)$, and dc offset with magnitude 0.08 p.u. are introduced at $t = 0.5$ s and the distortion is ended at $t = 0.7$ s. Considering this test case, the settling time of the proposed A-GDSC-PLL with the phase jump compensation scheme was 17 ms, while the convergence time reported by the authors was about 35 ms.
2) Unbalanced voltage with phase jump: At $t = 0.5$ s, the positive-sequence grid voltage has a phase jump of $+45°$, and a 0.3-p.u. FFNS component is added to it. At $t = 0.7$ s, the disturbance is ended. In this case, the results presented by the authors indicate a settling time of about 35 ms, while using the proposed technique, the settling time was around 20 ms.

A phase estimation algorithm (PEA), named as the WLSE-PEA, consisting of the moving average filter, the weighted least squares estimation (WLSE), the frequency-locked loop, and the zero crossing detection was proposed in [19]. Two results presented by the authors were reproduced using the proposed method for comparison. The WLSE-PEA's performance under phase jump, voltage sag, and frequency deviation were tested in a first case test. At 0.1 s, a 30° phase jump occurs on all the three phases; and at 0.3 s, there is a three-phase voltage sag (70%). The settling times reported by the authors and using our proposed technique were 11 and 6 ms for the first disturbance and 12 and 20 ms for the second disturbance, respectively. The WLSE-PEA's performance under odd-order harmonics as well as even-order harmonics is also compared with the proposed method. At 0.1 s, the harmonics imposed on the grid voltages include the third-order positive sequence, third-order negative sequence, fifth-order positive sequence, fifth-order negative sequence, seventh-order positive sequence, seventh-order negative sequence, ninth-order positive sequence, and ninth-order negative sequence (all 0.05 p.u., $-30°$, $70°$, $45°$, $50°$, $30°$, $30°$, $40°$, and $60°$, respectively). At 0.3 s, the grid voltages return to normal. At 0.5 s, the harmonics imposed on the grid voltages include the fourth-order negative sequence (0.01 p.u., $-60°$), sixth-order positive sequence (0.01 p.u., $30°$), and eighth-order negative sequence (0.01 p.u., $30°$). Considering the first disturbance, the settling times of the WSLE-PEA and of the proposed algorithm were 25 and 0 ms (the phase angle error did not reach $1°$), respectively. For the second disturbance, these settling times were both equal to 0 ms.

A fixed-gain filter (FGF) scheme with an optimal fixed feedback gain matrix to estimate the angle and frequency of the grid signal is presented in [20]. Instead of using the conventional PLL scheme, the concept of the Kalman filter is synthesized to design a second-order FGF and a third-order FGF for synchronization. In one of the test cases, the method was submitted to a $45°$ phase angle jump. According to the authors, using the implementation best suited for this case, the phase angle error converges to a 5% error band in 6.4 ms. Repeating this test case, we observed that using the proposed method, the angle error converged to a 2% error band in 6.2 ms.

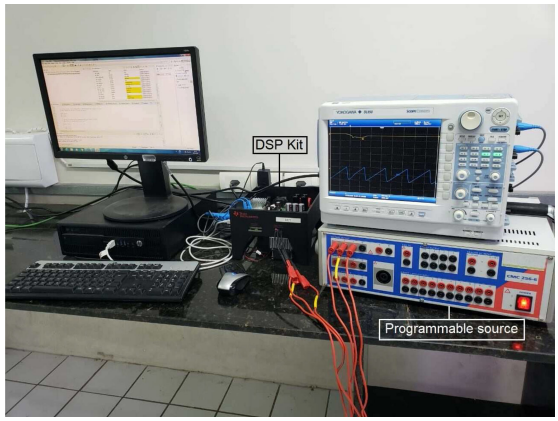

Fig. 15. Experimental prototype.

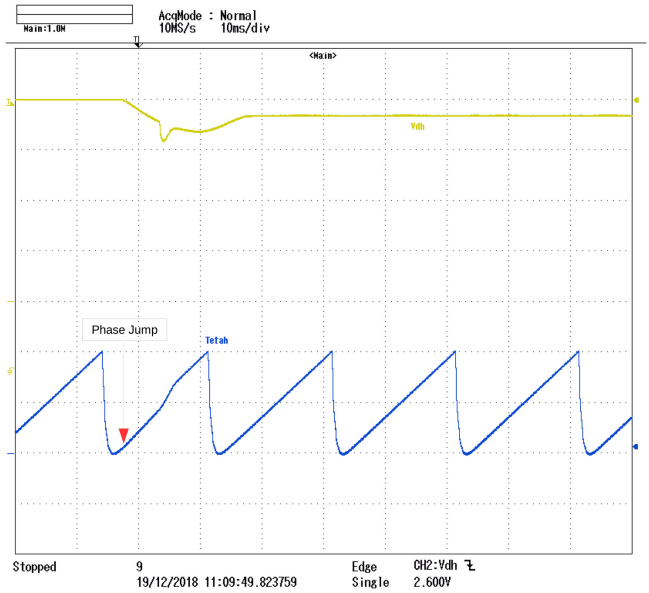

Fig. 16. Amplitude and phase angle of the FFPS component in Case 1.

VII. Experimental Results

In order to demonstrate the effectiveness of the proposed scheme, experimental results are provided in this section. The proposed A-GDSC-PLL with phase angle jump compensation was implemented in a prototype having a Texas Instruments TMS320F28335 DSP, with clock frequency $f_{\text{clk}} = 150$ MHz and sampling frequency $f_s = 15012.8$ kHz, being executed in approximately 43.2 μs, which corresponds to 55.3 % of the sampling period. The same test cases used in the simulations were also performed in the experiments, resulting in very similar responses. The experimental prototype is shown in Fig. 15.

The experimental prototype has only two pulsewidth modulation (PWM)-based digital-to-analog converters (DACs). The quantities chosen to be measured in each experiment were the amplitude and phase angle of the FFPS detected component. Figs. 16–18 show the experimental results corresponding to test cases 1–3, respectively. It can be observed that the dynamic

Authorized licensed use limited to: Universidad Federal de Pernambuco. Downloaded on September 28,2020 at 17:29:55 UTC from IEEE Xplore. Restrictions apply.

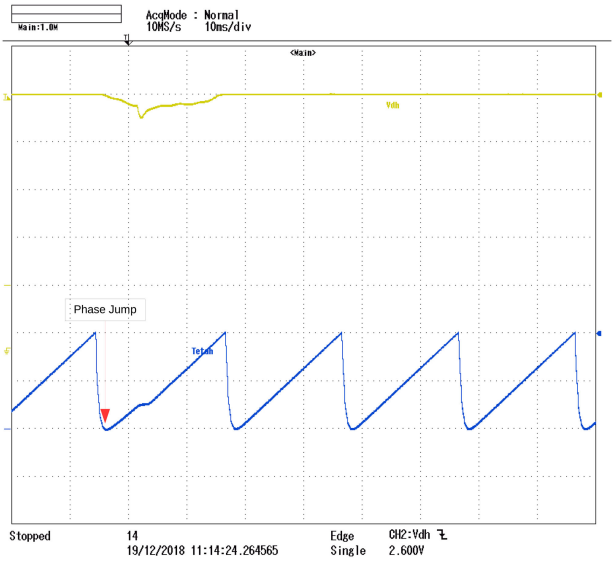

Fig. 17. Amplitude and phase angle of the FFPS component in Case 2.

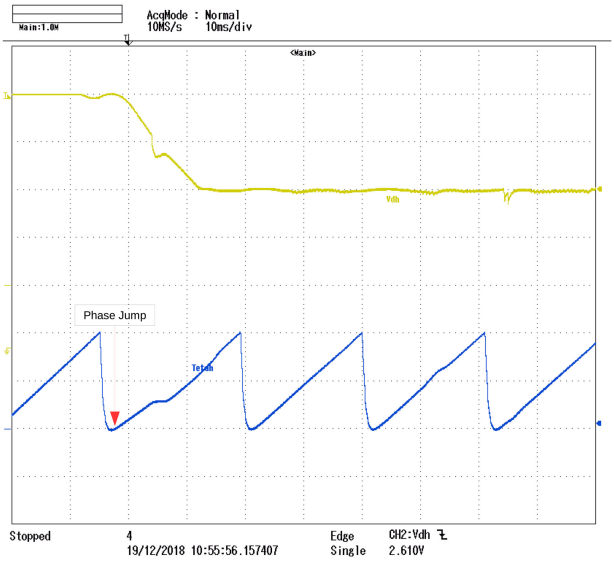

Fig. 18. Amplitude and phase angle of the FFPS component in Case 3.

of the response is in accordance with the simulation results. However, the response time cannot be precisely measured now, due to the DAC dynamic and its output low-pass filter (cut-off frequency of 328.8 Hz).

VIII. Conclusion

A study of the GDSC filter dynamics for signals subject to phase angle jumps, with or without other simultaneous disturbances, was performed. Through a mathematical analysis, it was demonstrated how to obtain the estimation of the phase angle jump during the GDSC transient as well as how to use it to accelerate the convergence of the SRF-PLL-based synchronization methods.

During the simulations, we show the improvement in the response time of the A-GDSC-PLL, even when frequency variations and dc components occur.

It was observed that, using the proposed method, the convergence time reduced about 50%, in comparison with the original A-GDSC-PLL. The proposed scheme works in all cases. However, for light disturbances, the performance of the proposed scheme may be similar to that of the A-GDSC-PLL, once the minimum phase jump sensitivity may not be reached.

Then, as long as the proposed method decreases the disturbances tracking time, we expect to improve the overall performance of the SRF-PLL based detection systems, such as in ultrafast protective relays.

References

[1] L. Asiminoael, F. Blaabjerg, and S. Hansen, "Detection is key-harmonic detection methods for active power filter applications," *IEEE Ind. Appl. Mag.*, vol. 13, no. 4, pp. 22–33, Jul./Aug. 2007.

[2] W. Li, X. Ruan, C. Bao, D. Pan, and X. Wang, "Grid synchronization systems of three-phase grid-connected power converters: A complex-vector-filter perspective," *IEEE Trans. Ind. Electron.*, vol. 61, no. 4, pp. 1855–1870, Apr. 2014.

[3] S. Golestan, J. M. Guerrero, and J. C. Vasquez, "Single-phase PLLs: A review of recent advances," *IEEE Trans. Power Electron.*, vol. 32, no. 12, pp. 9013–9030, Dec. 2017.

[4] S. Golestan, M. Monfared, F. D. Freijedo, and J. M. Guerrero, "Performance improvement of a prefiltered synchronous-reference-frame PLL by using a PID-type loop filter," *IEEE Trans. Ind. Electron.*, vol. 61, no. 7, pp. 3469–3479, Jul. 2014.

[5] D. Dong, B. Wen, D. Boroyevich, P. Mattavelli, and Y. Xue, "Analysis of phase-locked loop low-frequency stability in three-phase grid-connected power converters considering impedance interactions," *IEEE Trans. Ind. Electron.*, vol. 62, no. 1, pp. 310–321, Jan. 2015.

[6] V. Kaura and V. Blasko, "Operation of a phase locked loop system under distorted utility conditions," *IEEE Trans. Ind. Appl.*, vol. 33, no. 1, pp. 58–63, Jan./Feb. 1997.

[7] S.-K. Chung, "A phase tracking system for three phase utility interface inverters," *IEEE Trans. Power Electron.*, vol. 15, no. 3, pp. 431–438, May 2000.

[8] L. G. B. Rolim, D. R. Costa, and M. Aredes, "Analysis and software implementation of a robust synchronizing PLL circuit based on the pq theory," *IEEE Trans. Ind. Electron.*, vol. 53, no. 6, pp. 1919–1926, Dec. 2006.

[9] F. A. S. Neves, H. E. P. de Souza, M. C. Cavalcanti, F. Bradaschia, and E. J. Bueno, "Digital filters for fast harmonic sequence component separation of unbalanced and distorted three-phase signals," *IEEE Trans. Ind. Electron.*, vol. 59, no. 10, pp. 3847–3859, Oct. 2012.

[10] F. A. S. Neves, M. C. Cavalcanti, H. E. P. de Souza, F. Bradashia, E. J. Bueno, and M. Rizo, "A generalized delayed signal cancellation method for detecting fundamental-frequency positive-sequence three-phase signals," *IEEE Trans. Power Del.*, vol. 25, no. 3, pp. 1816–1825, Jul. 2010.

[11] Y. N. Batista, H. E. P. de Souza, F. A. S. Neves, R. F. Dias Filho, and F. Bradaschia, "Variable-structure generalized delayed signal cancellation PLL to improve convergence time," *IEEE Trans. Ind. Electron.*, vol. 62, no. 11, pp. 7146–7150, Nov. 2015.

[12] L. N. Arruda, S. M. Silva, and B. J. C. Filho, "PLL structures for utility connected systems," in *Proc. 36th Annu. Meeting IEEE Ind. Appl. Soc.*, Chicago, IL, USA, USA, 2001, pp. 2655–2660.

[13] H. E. P. de Souza, F. A. S. Neves, M. C. Cavalcanti, E. J. Bueno, and M. Rizo, "Frequency adaptive phase-sequence separation method based on a generalized delayed signal cancelation method," in *Proc. Energy Convers. Congr. Expo.*, San Jose, CA, USA, 2009, pp. 568–572.

[14] S. Buso and P. Mattavelli, *Digital Control in Power Electronics* (Synthesis Lectures on Power Electronics), vol. 1. San Rafael, CA, USA: Morgan & Claypool, 2006.

[15] P. Mattavelli, "An improved deadbeat control for UPS using disturbance observers," *IEEE Trans. Ind. Electron.*, vol. 52, no. 1, pp. 206–212, Feb. 2005.

[16] Y. A.-R. I. Mohamed and E. F. El-Saadany, "An improved deadbeat current control scheme with a novel adaptive self-tuning load model for a three-phase PWM voltage-source inverter," *IEEE Trans. Ind. Electron.*, vol. 54, no. 2, pp. 747–759, Apr. 2007.

[17] S. Golestan, M. Monfared, and F. D. Freijedo, "Design-oriented study of advanced synchronous reference frame phase-locked loops," *IEEE Trans. Power Electron.*, vol. 28, no. 2, pp. 765–778, Jun. 2013.

Authorized licensed use limited to: Universidad Federal de Pernambuco. Downloaded on September 28,2020 at 17:29:55 UTC from IEEE Xplore. Restrictions apply.

[18] S. Gude and C. Chu, "Dynamic performance improvement of multiple delayed signal cancelation filters based three-phase enhanced-PLL," *IEEE Trans. Ind. Appl.*, vol. 54, no. 5, pp. 5293–5305, Sep. 2018.
[19] L. Zheng, H. Geng, and G. Yang, "Fast and robust phase estimation algorithm for heavily distorted grid conditions," *IEEE Trans. Ind. Electron.*, vol. 63, no. 11, pp. 6845–6855, Nov. 2016.
[20] X. Cai, C. Wang, and R. Kennel, "A fast and precise grid synchronization method based on fixed-gain filter," *IEEE Trans. Ind. Electron.*, vol. 65, no. 9, pp. 7119–7128, Sep. 2018.

Daniel Soares dos Santos Andrade was born in Paulista, Brazil, in 1988. He received the B.S. degree in electrical engineering from Pernambuco State University, Recife, Brazil, in 2011, and the M.Sc. degree in 2018 from the Federal University of Pernambuco, Recife, where he is currently working toward the Ph.D. degree in electrical engineering with the Federal University of Pernambuco.

Since 2013, he has been with the Federal Rural University of Pernambuco. His research interests include power quality and grid synchronization methods.

Ygo Neto Batista was born in Recife, Brazil, in 1982. He received the B.S. degree in electrical engineering, the M.Sc. degree in computer science, and the Ph.D. degree in electrical engineering from the Federal University of Pernambuco, Recife, in 2007, 2011 and 2018, respectively.

Since 2009, he has been with the Department of Industry, Federal Institute for Education, Science and Technology of Pernambuco, Recife. His research interests include power quality and grid synchronization methods.

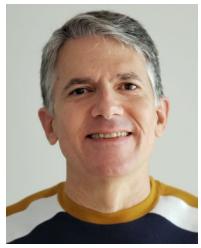

Francisco A. S. Neves (M'00–SM'13) was born in Campina Grande, Brazil, in 1963. He received the B.S. and M.Sc. degrees in electrical engineering from the Federal University of Pernambuco, Recife, Brazil, in 1984 and 1992, respectively, and the Ph.D. degree in electrical engineering from the Federal University of Minas Gerais, Belo Horizonte, Brazil, in 1999.

He worked as a Visiting Scholar with the Georgia Institute of Technology, Atlanta, GA, USA, in 1999, and with the University of Alcala, Spain, from 2008 to 2009. Since 1993, he has been with the Department of Electrical Engineering, Federal University of Pernambuco, where he is a Professor of Electrical Engineering. His research interests include power electronics, renewable energy systems, power quality and grid-connected converter.

Prof. Neves was the co-recipient of the Best Paper Award in two IEEE conferences: the International Conference on Power Electronics and Intelligent Control for Energy Conservation, in 2005 and the International Symposium on Industrial Electronics, in 2011.

Helber Elias Paz de Souza was born in Cabo de Santo Agostinho, Brazil, in 1983. He received the B.S., M.Sc., and Ph.D. degrees in electrical engineering from the Federal University of Pernambuco, Recife, Brazil, in 2006, 2008, and 2012, respectively.

Since 2009, he has been with the Department of Industry, Federal Institute for Education, Science and Technology of Pernambuco. His research interests include power quality and grid synchronization methods.

Authorized licensed use limited to: Universidad Federal de Pernambuco. Downloaded on September 28,2020 at 17:29:55 UTC from IEEE Xplore. Restrictions apply.